

CMOS-compatible Strain Engineering for High-Performance Monolayer Semiconductor Transistors

Marc Jaikissoon¹, Çağıl Köroğlu¹, Jerry A. Yang¹, Kathryn M. Neilson¹, Krishna C. Saraswat^{1,2}, Eric Pop^{1,2,3,*}

¹*Department of Electrical Engineering, Stanford University, Stanford, CA 94305, U.S.A.*

²*Department of Materials Science & Engineering, Stanford University, Stanford, CA 94305, U.S.A.*

³*Precourt Institute for Energy, Stanford University, Stanford, CA 94305, U.S.A.*

*Corresponding author email: epop@stanford.edu

Strain engineering has played a key role in modern silicon electronics, having been introduced as a mobility booster in the 1990s and commercialized in the early 2000s. Achieving similar advances with two-dimensional (2D) semiconductors in a CMOS (complementary metal oxide semiconductor) compatible manner would radically improve the industrial viability of 2D transistors. Here, we show silicon nitride capping layers can impart strain to monolayer MoS₂ transistors on conventional silicon substrates, enhancing their electrical performance with a low thermal budget (350 °C), CMOS-compatible approach. Strained back-gated and dual-gated MoS₂ transistors demonstrate median increases up to 60% and 45% in on-state current, respectively. The greatest improvements are found when both transistor channels and contacts are reduced to ~200 nm, reaching saturation currents of 488 $\mu\text{A}/\mu\text{m}$, higher than any previous reports at such short contact pitch. Simulations reveal that most benefits arise from tensile strain lowering the contact Schottky barriers, and that further reducing device dimensions (including contacts) will continue to offer increased strain and performance improvements.

Commercial silicon CMOS technology has benefitted from strain boosting of transistor performance for two decades, since the 90 nm technology node¹⁻⁵. Silicon nitride (SiN_x) capping layers have been used in silicon nMOS to achieve uniaxial tensile strain and increase electron mobility^{6,7}, whereas selective SiGe growth in the silicon pMOS source and drain has been used to create uniaxial compressive strain and enhance hole mobility⁸. These improvements are due to changes in the band structure, which lead to a reduction of electron and hole effective masses and scattering rates.

Two-dimensional (2D) semiconductors such as transition metal dichalcogenides (TMDs) have gained recent attention due to their atomically thin nature, which shows potential for transistor scaling⁹. TMDs like monolayer molybdenum disulfide (MoS₂) have seen several advances in growth^{10,11}, doping^{12,13}, and contact engineering¹⁴⁻¹⁶ for transistor applications. As with silicon, strain engineering has been

predicted to modulate the TMD band structure and mobility¹⁷⁻¹⁹, however these effects have only been probed through optical experiments^{20,21}, or electrical measurements of micron-scale monolayers on bent flexible substrates²² and bilayers on rigid substrates²³. To fundamentally enable the integration of TMD transistors with conventional semiconductor technology, strain must be implemented in scalable, CMOS-compatible ways on planar, rigid silicon substrates, ideally boosting the performance of nanoscale monolayer transistors, closer to the fundamental limits of these materials.

Silicon Nitride Deposition and Back-Gated Devices

In this work, we apply controllable strain to monolayer MoS₂ by depositing SiN_x films with high (yet tunable) intrinsic tensile stress by plasma-enhanced chemical vapor deposition (PE-CVD) at 350 °C. Owing to the low deposition temperature used, this is an attractive back-end-of-line (BEOL) compatible approach, with SiN_x being widely employed in modern semiconductor technology²⁴. The stress in these films can be varied from compressive to tensile by varying deposition parameters such as precursor ratio, He gas dilution and pressure²⁵. This offers process tunability using a single capping layer, rather than needing separate materials to select between compressive and tensile stress. (Further details of SiN_x deposition and stress tuning are provided in **Supplementary Information Section 1**.)

To understand the strain effects of SiN_x capping on a simplified device geometry, we first examine a conventional back-gated structure, as shown in **Figure 1a**. Monolayer MoS₂ is grown by CVD on 90 nm SiO₂ on p⁺⁺ Si substrates²⁶, which also serve as back-gates. The contact metal is 50 nm of Au deposited by electron-beam (e-beam) evaporation at a pressure of $\sim 10^{-8}$ Torr, and further details regarding device fabrication are given in the Methods. **Figure 1b** shows that plasma-induced damage occurs when SiN_x films are directly deposited on MoS₂, as indicated by the appearance of the defect-induced LA(M) peak²⁷ in the Raman spectra of MoS₂. Thus, we use a barrier layer of 1.5 nm e-beam evaporated Al followed by 10 nm AlO_x deposited by atomic layer deposition (ALD), which is a common encapsulation¹² for monolayer MoS₂. **Figure 1c** shows that when SiN_x is deposited after AlO_x, the Raman characteristics of MoS₂ do not display visible defect signatures. However, we note that Raman analysis cannot be used to accurately estimate strain in such encapsulated MoS₂, because doping and plasmon coupling from the AlO_x also affect the E' peak position²⁸. Instead we rely on grazing incidence X-ray diffraction measurements for blanket films (**Supplementary Information Section 2**) and finite-element simulations of strain distributions in nanoscale devices, further below.

The effect of stressor layers has been shown to depend strongly on the critical dimensions of the device for Si nMOS, with shorter channels experiencing higher strains after capping²⁹. For this reason, we

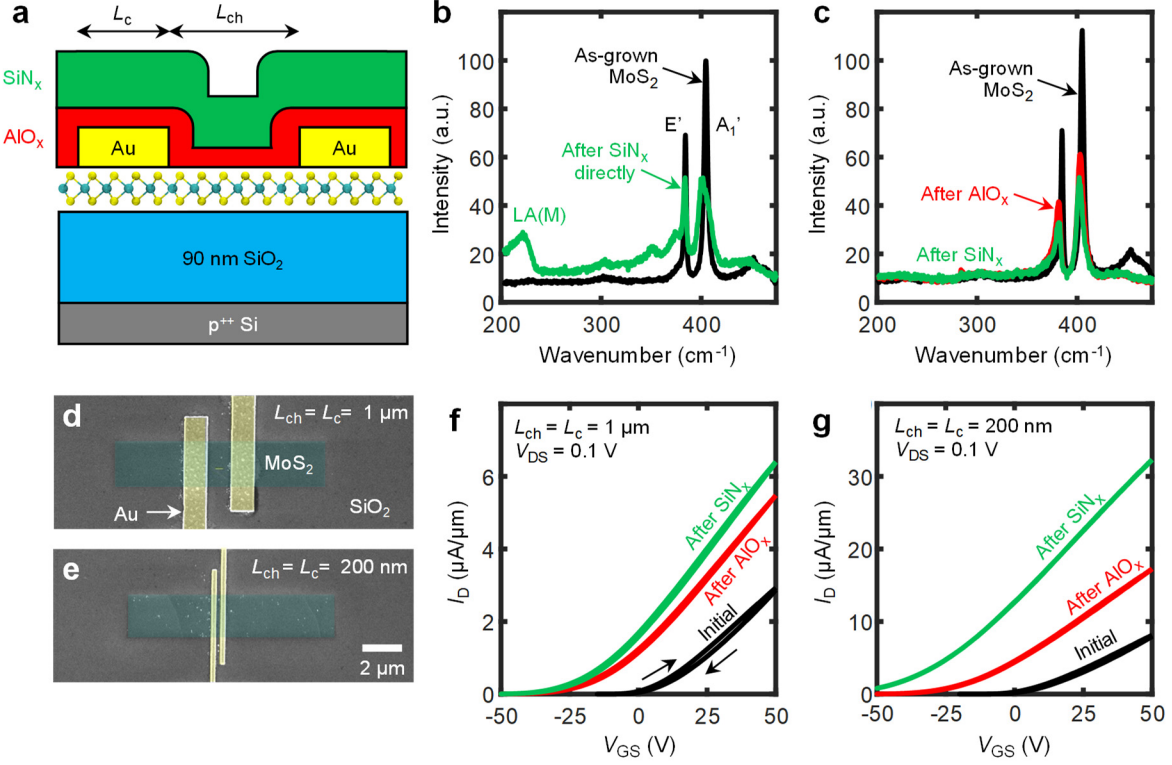


Fig. 1 | Back-gated transistor characterization. **a**, Schematic of back-gated monolayer MoS₂ transistor capped with AlO_x and tensile-stressed SiN_x. The contact pitch is the sum of channel and contact length, CP = $L_{ch} + L_c$. Raman spectra of monolayer MoS₂ before and after direct deposition of SiN_x: **b**, without AlO_x buffer layer and **c**, with AlO_x buffer. Top-down, false color scanning electron microscope image of **d**, ‘long’ device with $L_{ch} = L_c = 1 \mu\text{m}$ and **e**, a ‘short’ device with $L_{ch} = L_c = 200 \text{ nm}$. **f**, Back-gated transfer characteristics of high-stress SiN_x-capped MoS₂ transistor with ‘long’ dimensions and **g**, ‘short’ dimensions. Small arrows mark forward and backward voltage sweeps.

investigate the effect of device dimensions by varying the length of the channel (L_{ch}) and contacts (L_c), using ‘long’ and ‘short’ geometries with $L_{ch} = L_c$ of 1 μm and 200 nm, respectively, as shown in **Figure 1d,e**. To understand the effect of capping layers, we performed electrical measurements on the same devices after each step: initial (no capping), after AlO_x is deposited, and after SiN_x is deposited. This allows us to avoid variability which may occur from using different MoS₂ growths.

Figure 1f,g shows the measured drain current vs. gate voltage (I_D - V_{GS}) of ‘long’ and ‘short’ devices, respectively. In both cases, the AlO_x layer induces n -type doping as previously reported^{12,30}, negatively shifting the threshold voltage (V_T) and lowering the contact resistance. On the other hand, capping with SiN_x (75 nm thick, ~600 MPa tensile stress) is noticeably geometry-dependent: the ‘long’ device has only a small negative V_T shift, while the ‘short’ device displays both a larger V_T shift, as well as im-

proved transconductance ($g_m = \partial I_D / \partial V_{GS}$) and on-state current (I_{on}). While the V_T shift could be attributed to doping from the capping layers, the geometry dependence and improved transconductance point to an origin of this enhancement arising from the stressed SiN_x , as we investigate below.

We first confirm that the improvement is reproducible by measuring several (6 to 10) devices with both ‘long’ and ‘short’ geometries, as shown with box plots in **Figure 2a,b**. To account for V_T shifting,

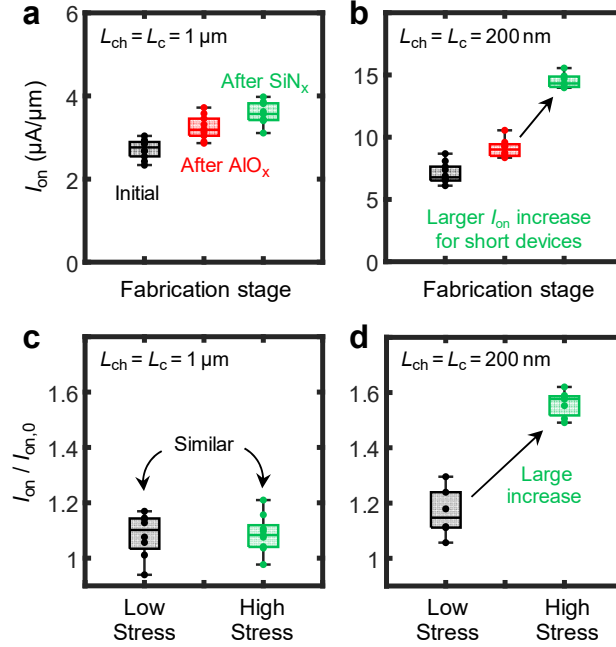


Fig. 2 | Geometry-dependent device statistics and low-stress control sample. Box plots of normalized on-state current (I_{on}) at $n = 8 \times 10^{12} \text{ cm}^{-2}$ for several devices, after each fabrication step. **a**, $L_{ch} = L_c = 1 \mu\text{m}$ (‘long’) and **b**, $L_{ch} = L_c = 200 \text{ nm}$ (‘short’) devices. Relative improvement in I_{on} after capping with low- (50 to 100 MPa) and high-stress (600 MPa) SiN_x films for **c**, ‘long’ and **d**, ‘short’ devices. All measurements are carried out at room temperature and $V_{DS} = 0.1 \text{ V}$.

I_{on} is extracted at a carrier density of $n \approx 8 \times 10^{12} \text{ cm}^{-2}$. The median I_{on} increases by 14% in ‘long’ devices after SiN_x capping (**Figure 2a**) and by 60% in ‘short’ devices (**Figure 2b**). This demonstrates that the effect of high-stress capping is consistent between devices of the same type, with larger increases of I_{on} observed only for the smaller geometry. Other combinations of channel and contact length are shown in **Supplementary Information Section 3**, confirming that both dimensions must be reduced to maximize the I_{on} improvement from this technique. These findings are consistent with those from silicon technology, where greater strain-induced performance (I_{on}) is also found in smaller devices²⁹.

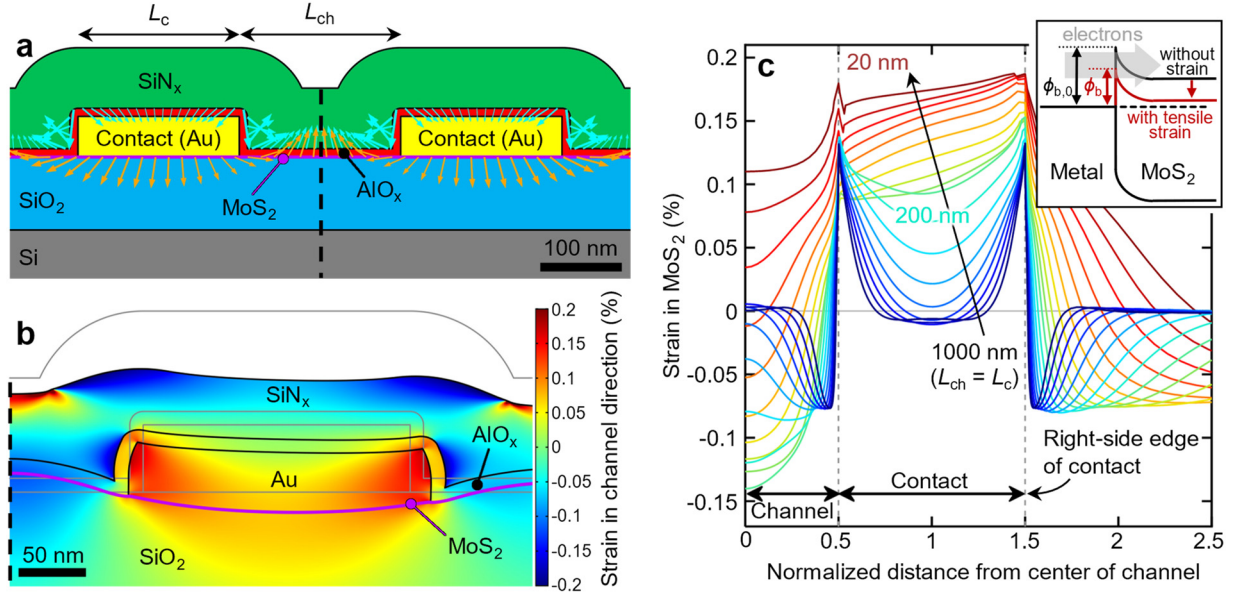


Fig. 3 | Strain simulations. **a**, Cross-section of the ‘short’ device with $L_{ch} = L_c = 200$ nm. The horizontal magenta line shows the location of the monolayer MoS₂. Cyan arrows indicate the traction applied by the SiN_x stressor layer on the underlying AlO_x. Orange arrows indicate the displacement of MoS₂ after the structure is allowed to relax. The dashed line marks the center of the device, i.e. the symmetry plane. **b**, Zoom into the simulated right-side contact region, with heat map denoting the horizontal strain field (tensile strain is positive). Deformations are exaggerated by a factor of 200. Gray lines are material boundaries prior to deformation. **c**, Strain profile along horizontal direction for devices with $L_{ch} = L_c$ from 1 μm down to 20 nm. Note that distances are normalized by the channel length. Inset: effect of tensile strain on the Schottky barrier at the MoS₂ contact.

Next, we fabricate control samples by capping with a low-stress (50 to 100 MPa) SiN_x layer of the same thickness and deposition temperature as the high-stress (600 MPa) SiN_x described above. **Figure 2c,d** compares the effect of different stress levels on the relative $I_{on}/I_{on,0}$ at $n \approx 8 \times 10^{12} \text{ cm}^{-2}$ for both device geometries. (Here, $I_{on,0}$ is the current level after the AlO_x buffer but before SiN_x capping.) For ‘long’ devices (**Figure 2c**), both low- and high-stress SiN_x layers lead to similar results, with only a small improvement ($\sim 10\%$) of median I_{on} . However, for ‘short’ devices, **Figure 2d** shows that capping with high-stress SiN_x increases the median I_{on} by nearly $\sim 60\%$, compared to 18% with the low-stress SiN_x. This confirms that the large improvement originates from the high tensile stress SiN_x, rather than annealing or doping effects which would be similar for both low- and high-stress capping.

Finite Element Simulations of Strain Profile

To understand the origin of the performance enhancement achieved with high-stress SiN_x, we performed finite-element method simulations of such BG devices with various channel and contact lengths

to compute the strain distribution. **Figure 3a** shows the ‘short’ 200-nm device cross-section, with arrows indicating the traction applied by the SiN_x on the underlying AlO_x, as well as the resulting displacement field of MoS₂. A zoomed-in, exaggerated deformation of the right contact and a color map of the strain field along the channel direction are shown in **Figure 3b**. The tensile SiN_x ‘pushes down’ on the contact, while simultaneously ‘pulling’ on its bottom corners³¹, like a taut tape simultaneously squeezing and pulling on a small object placed beneath. (See **Supplementary Information Figure 4** for a simple representation of this effect using tape, a drinking straw, and a kitchen sponge.)

Thus, the tensile SiN_x layer imparts a complex, non-uniform strain profile along the MoS₂ contact and channel, with uniaxial tensile strain under the contact and compressive strain in the channel, as shown in **Figure 3c**. (More simulation details are included in **Supplementary Information Section 5**.) This figure plots the strain along MoS₂ for several cases of $L_{\text{ch}} = L_c$, from 1 μm to 20 nm. At longer dimensions ($L_{\text{ch}} = L_c > 150$ nm), the tensile strain under the contact is highest near the edges, decaying toward the center of the contact with a characteristic length of ~ 120 nm, and the compressive strain in the channel is highest near the contact. We estimate tensile strains between 0.1–0.2% near the contact, although we note that factors such as thermal expansion during SiN_x deposition, changes in the elastic modulus of MoS₂ due to defects, increases in the SiN_x stress during pre-measurement annealing and slipping between the MoS₂ and the substrate can act to increase this strain value in devices. As dimensions are reduced, the tensile strain under the contact increases and becomes more uniform, and the channel strain eventually becomes tensile as well. (Additional trends are explored in more detail in **Supplementary Information Sections 6 and 7**.) Based on these projections, we expect that this technique offers the most benefit at sub-50 nm contact pitches, where both the channel and contact resistances can be greatly improved.

Tensile (compressive) strain distribution in or under mesa-like structures capped with tensile (compressive) stressors have been noted in the silicon literature^{31,32} and exploited to enhance the device performance²⁹. For a 2D semiconductor like MoS₂, tensile strain is expected to lower the K-valley of the conduction band^{18,22}, bringing it closer to the Fermi level under our contacts and reducing the Schottky barrier height³³ (see **Figure 3c inset**). In addition, the ‘downward’ pressure exerted by the tensile-strained contacts on the MoS₂ (**Supplementary Information Section 8**) could reduce the metal-MoS₂ van der Waals gap at the contact^{34,35}, improving electron tunneling. The corresponding reduction of contact resistance is the likely mechanism for the performance enhancement seen in our devices capped with high tensile stress SiN_x, with the greatest enhancement seen in our ‘short’ (more

contact-dominated) devices (**Figure 2d**). Importantly, we also find that additional performance enhancements are possible as the channel and contact lengths are scaled down toward 20 nm, due to increased strain under the contacts as well as the channel going from compressive to tensile strained which could significantly increase the channel mobility^{18,22}.

To experimentally examine the effect of stress on the contacts, we estimate the Schottky barrier height of devices capped with high tensile-stressed SiN_x. As shown in **Supplementary Information Section 9**, we extract an effective barrier of ~60 meV, which is significantly lower than our control sample measurements and other values from the literature (120-150 meV)³⁶. We also perform a pseudo-transfer length method analysis (see **Supplementary Information Section 10**), which confirms that devices with ‘short’ dimensions exhibit lower contact resistance. These results corroborate the findings of our finite element simulations, showing how strain can be used for CMOS-compatible contact engineering in TMDs.

Strained Dual-Gate Field-Effect Transistors

Finally, we extend our strain technique to dual-gated (DG) transistors (schematic in **Figure 4a**), which have a Pd top gate (TG) above the AlO_x encapsulation layer described earlier. As with the earlier BG transistors, we fabricate devices with different values of L_{ch} and L_c , and measure their electrical characteristics before and after capping with the SiN_x stress layer above the TG. The scanning electron microscope image of an encapsulated ‘short’ device ($L_{ch} = L_c = 200$ nm) is shown in **Figure 4b**. For optimal control of the transistor characteristics, we sweep both TG and BG voltages simultaneously, but with different ranges and voltage steps due to the unequal top and back-gate dielectrics.

Figure 4c displays electrical measurements of such a ‘short’ device. After high-tensile stress SiN_x capping, I_{on} increases by 33% (at maximum V_{BG} and V_{TG} applied), with only a small negative V_T shift. Any possible charge transfer doping from the SiN_x encapsulation is effectively blocked by the top-gate, which fully overlaps the channel and contacts. The transconductance (slope, g_m) itself increases by 32% after SiN_x, underlining that the higher I_{on} is almost entirely due to strain-induced improvements in mobility and contact resistance. Small V_T shifts due to strain are not unexpected (due to changes in the band gap) and have also been observed in silicon technology³⁷, but can be compensated by gate stack engineering³⁸. In addition, the larger band gap of monolayer TMDs (~ 2× larger than Si) implies that any trade-offs in off-state current will be easier to manage than in silicon.

The output characteristics in **Figure 4d** reveal a saturation current of $I_{D,sat} = 488 \mu\text{A}/\mu\text{m}$ (394 $\mu\text{A}/\mu\text{m}$) at $V_{DS} = 2$ V (1 V), the highest reported to date in a 200 nm monolayer MoS₂ channel (with 400 nm

contact pitch), in a device without otherwise optimized metal contacts or gate dielectrics. This is an important finding, which signifies that strained (but otherwise ordinary) contacts can yield device performance similar to the best Bi or Sb contacts available today^{14,15}. The CMOS-compatible strain approach employed in this work is agnostic to the type of contacts, opening the door to future device optimization with more industry-friendly metals.

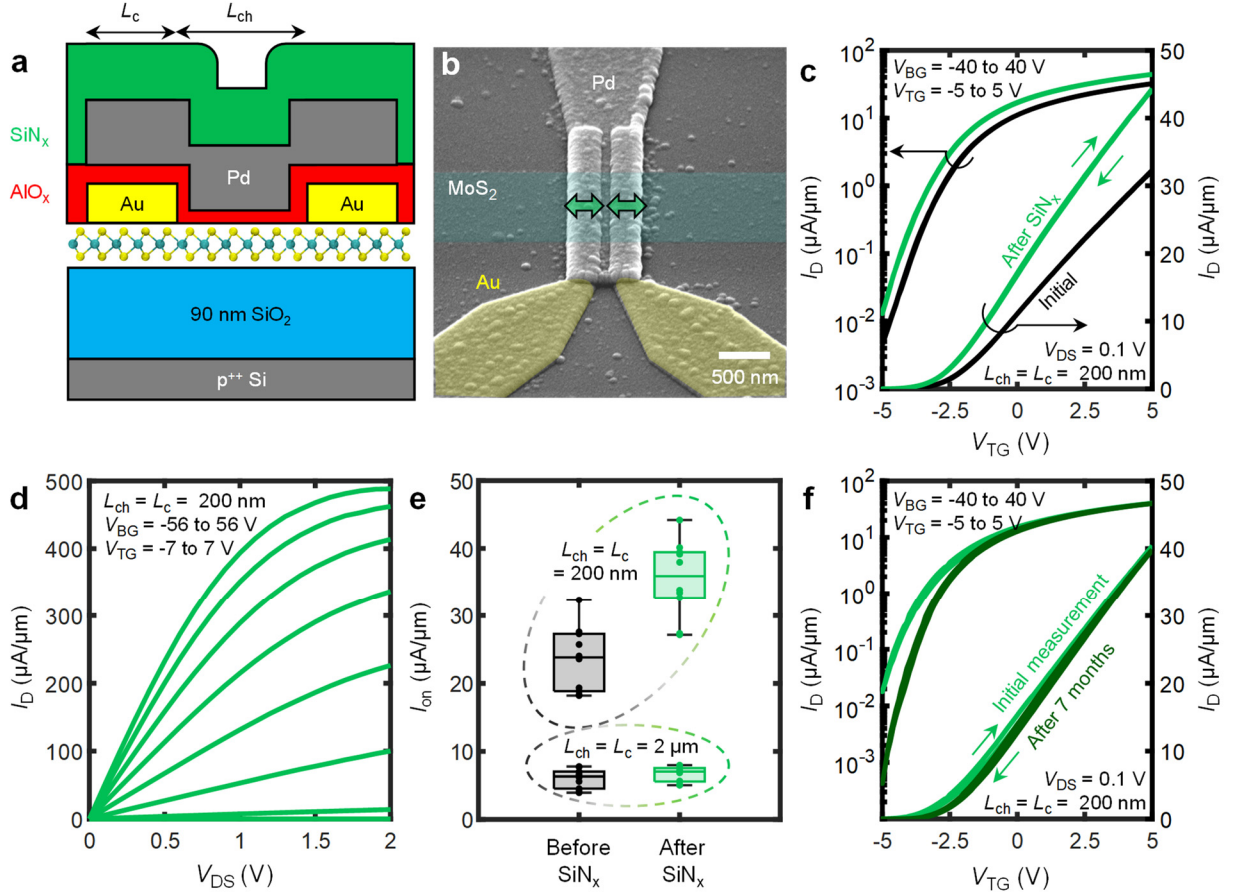


Fig. 4 | Dual-gated transistors with strain. **a**, Schematic of device structure for a dual-gated (TG and BG) monolayer (1L) MoS₂ transistor capped with AlO_x and tensile stressed SiN_x. **b**, Tilted, colored scanning electron microscope image of a 'short' device with channel and contact length of 200 nm. The top Pd gate overlaps both source and drain contacts. The green block arrows represent the tensile-stressed SiN_x capping. **c**, Transfer characteristics for a dual-gated high-stress (~800 MPa) SiN_x-capped monolayer MoS₂ transistor with dimensions $L_{ch} = L_c = 200$ nm. **d**, Output characteristics after SiN_x capping, displaying on-state current of $I_{D,sat} = 488 \mu\text{A}/\mu\text{m}$ (with proper saturation at $V_{DS} = 2$ V) when both top and bottom gates are set to high bias. Each voltage step is 16 V on the back gate, and 2 V on the top gate. **e**, Box plots summarizing the change in I_{on} at $V_{DS} = 0.1$ V for DG devices with 'long' and 'short' dimensions after SiN_x capping **f**, Transfer characteristics of a SiN_x-capped device after 7 months, showing no visible degradation of the on-state current. Measurements were performed in air, at room temperature. Small arrows mark forward and backward sweeps³⁹, showing minimal hysteresis over this voltage range, with SiN_x encapsulation. For both **c** and **f**, the V_{BG} and V_{TG} step size have a ratio of 8:1, proportional to their respective voltage sweep ranges.

We summarize measurements of several DG transistors with the ‘short’ (200 nm) and ‘long’ (2 μm) geometry in **Figure 4e**. For ‘long’ devices, I_{on} increases only a few percent after high-stress capping. In contrast, ‘short’ devices display a large median I_{on} increase of 45%. This effect is reproducible across all measured transistors and confirms our BG device findings (**Figures 2 and 3**), that strain boosts the performance of transistors with smaller channel length and contact pitch (here, 200 nm and 400 nm, respectively). Our DG simulations in **Supplementary Information Section 6** show similar strain distributions as in BG transistors, indicating the performance increase is primarily due to tensile contact strain, and projecting further enhancement in smaller devices. These simulations provide possible design guidelines on how the TMD device geometry can be tailored to maximize the benefit of strain to either contact or channel resistance individually, or simultaneously.

We also test the stability of our method by measuring transistor characteristics over time, as shown in **Figure 4f**. After 7 months, the device shows no degradation of on-state current even when these measurements are performed in air, illustrating that SiN_x also offers robust encapsulation, which has been well-studied in Si transistors as a diffusion barrier to moisture and gases^{24,40}. Our CMOS-compatible strain technique can also be applied to other TMDs which are expected to benefit from tensile strain¹⁷, such as monolayer WSe_2 (see **Supplementary Information Section 11**). We anticipate that this approach will offer further improvements to 2D transistors with even shorter critical dimensions, paving the way for the implementation of CMOS-compatible strain in high-performance TMDs.

Conclusions

We have reported the first CMOS-compatible approach to impart strain to 2D semiconductor transistors, using low-temperature, tensile-stressed silicon nitride capping layers. This improves the performance of monolayer MoS_2 transistors up to 60%, reaching saturation current of 488 $\mu\text{A}/\mu\text{m}$, a record at a contact pitch of just 400 nm (channel + contact). Simulations reveal that strain is expected to have even greater benefits in future transistors with smaller contact pitches, e.g. sub-50 nm. The results of this study are essential for integrating 2D semiconductors into future electronics, and this work is also likely to motivate future exploration of strain engineering in other next-generation semiconductors.

Methods

Device Fabrication. Monolayer MoS_2 was synthesized by chemical vapor deposition (CVD) at 750 $^\circ\text{C}$ directly onto thermally-grown SiO_2 (90 nm) on 1.5 cm \times 2 cm p^{++} silicon substrates, as previously reported²⁶. For back-gated (BG) devices, MoS_2 was used directly on the growth substrates, where the p^{++} Si also serves as BG. Electron-beam (e-beam) lithography (Raith VOYAGER) was employed for

each patterning step, using poly(methyl methacrylate) (PMMA) as e-beam resist to minimize potential delamination from aqueous developers used in photolithography. First, alignment marks (2 nm Ti/40 nm Au) were patterned and deposited by lift-off after e-beam evaporation. Discrete single-crystal MoS₂ triangles were identified under a microscope and lithography masks were designed such that each device was fabricated within a single triangle of MoS₂, in regions with minimal overgrowth. The channel dimensions were then defined using XeF₂ etching for 90 s at 3 Torr (Xactix e-1). Large probing pads (20 nm SiO₂/2 nm Ti/20 nm Pt) were then patterned and deposited via lift-off, with the evaporated SiO₂ layer serving to reduce potential leakage to the back-gate. Finally, source and drain device contacts (50 nm Au without an adhesion layer¹⁶) were used to connect the MoS₂ channels with the probing pads, patterned and deposited by lift-off using e-beam evaporation at $< 5 \times 10^{-8}$ Torr and a rate of 0.5 Å/s. All lift-off processes were performed in acetone for a minimum of 2 hours.

Next, e-beam evaporation was used to deposit a 1.5 nm Al film¹² onto of finished BG devices, with Al oxidizing in air to sub-stoichiometric AlO_x. Subsequently, 10 nm Al₂O₃ is deposited by atomic layer deposition at 200 °C (Cambridge Nanotech Savannah S200). This serves as the barrier layer prior to SiN_x capping for BG devices, and as the top-gate insulator for DG devices. At this stage, the Al₂O₃ is wet-etched (JT-Baker, Aluminum etch) over the contact pads after optical lithography. BG devices are then encapsulated by SiN_x, which is removed only over the contact pads after optical lithography and CF₄ plasma etching (Samco PC300). For DG devices, e-beam lithography is used to define the gate metal (50 nm Pd) via lift-off, followed by SiN_x deposition and contact access as described above.

All transistors were tested with a Keithley 4200 semiconductor parameter analyzer. BG transistors are measured in a Janis ST-500 probe station under $\sim 10^{-5}$ Torr vacuum after *in-situ* annealing at 250 °C for 2 hours. DG transistors are measured in air due to minimal hysteresis after encapsulation. All measurements are done at room temperature unless otherwise stated.

Silicon Nitride Deposition. Silicon nitride (SiN_x) was deposited using plasma-enhanced CVD (PECVD) in a PlasmaTherm Shuttlelock PECVD system using SiH₄ (5% in He) and NH₃ gases. Several recipes were developed in order to control the resultant film stress, and it was found that the major process variable which can be used to control stress is the ratio of NH₃ to SiH₄. At higher ratios of NH₃:SiH₄ > 1 film stress becomes tensile, whereas lower ratios promote compressive stress (see **Supplementary Information Section 1** for more details). Additionally, the amount of He in the process chamber can be used to further tune the stress if needed. For the transistors in this work, the deposition temperature was set to 350 °C although this can be reduced as low as 130 °C, both temperatures being

back-end of line (BEOL) compatible. Deposition powers were tuned from 20 to 100 W, with process pressures between 1 to 2 Torr resulting in deposition rates between 10 to 15 nm/min. Films were characterized using ellipsometry to precisely fit both refractive index and thickness in order to obtain accurate information about the deposition, which is necessary for accurate stress measurement. Film stress was measured on reference 4" silicon wafers using a Flexus 2320 Stress Tester via radius of curvature measurements before and after deposition.

References

- (1) Thompson, S.; Anand, N.; Armstrong, M.; Auth, C.; Alavi, M.; Bai, P.; Bielefeld, I.; Bigwood, R.; Buehler, M.; Cea, S.; Chikarmane, V.; Choi, C.; Frankovic, R.; Ghani, T.; Glass, G.; Han, W.; Hoffmann, T.; Hussein, M.; Jacob, P.; Jain, A. C.; Joshi, S.; Kenyon, C.; Klaus, I.; Klopčič, S.; Luce, I.; McIntyre, B.; Misty, K.; Munhy, A.; Nguyen Pearson, P. H.; Sandford, T.; Schweinfurh, R.; Shah, R.; Siv, S.; Taylor, M.; Tufts, B.; Wallace, C.; Wang, P.; Weber, C.; Bohr, M. A 90 nm Logic Technology Featuring 50 nm Strained Silicon Channel Transistors, 7 Layers of Cu Interconnects, Low k ILD, and 1 μm^2 SRAM Cell. *IEEE International Electron Devices Meeting* **2002**, 61–64.
- (2) Ghani, T.; Armstrong, M.; Auth, C.; Bost, M.; Charvat, P.; Glass, G.; Hoffmann, T.; Johnson, K.; Kenyon, C.; Klaus, J.; McIntyre, B.; Mistry, K.; Murthy, A.; Sandford, J.; Silberstein, M.; Sivakumar, S.; Smith, P.; Zawadzki, K.; Thompson, S.; Bohr, M. A 90 nm High Volume Manufacturing Logic Technology Featuring Novel 45 nm Gate Length Strained Silicon CMOS Transistors. *IEEE International Electron Devices Meeting* **2003**, 978–980.
- (3) Welser, J.; Hoyt, J.; Gibbons, J. NMOS and PMOS Transistors Fabricated in Strained Silicon/Relaxed Silicon-Germanium Structures. *IEEE International Electron Devices Meeting* **1992**, 1000–1002.
- (4) Rim, K.; Hoyt, J. L.; Gibbons, J. F. Transconductance Enhancement in Deep Submicron Strained-Si n-MOSFETs. *IEEE International Electron Devices Meeting* **1998**, 707–710.
- (5) Takagi, S. I.; Hoyt, J. L.; Welser, J. J.; Gibbons, J. F. Comparative Study of Phonon-Limited Mobility of Two-Dimensional Electrons in Strained and Unstrained Si Metal-Oxide-Semiconductor Field-Effect Transistors. *J Appl Phys* **1996**, *80*, 1567–1577.
- (6) Ito, S.; Namba, H.; Yamaguchi, K.; Hirata, T.; Ando, K.; Koyama, S.; Kuroki, S.; Ikezawa, N.; Suzuki, T.; Saitoh, T.; Horiuchi, T. Mechanical Stress Effect of Etch-Stop Nitride and Its Impact on Deep Submicron Transistor Design. *IEEE International Electron Devices Meeting* **2000**, 247–250.
- (7) Shimizu, A.; Hachimine, K.; Ohki, N.; Ohta, H.; Koguchi, M.; Nonaka, Y.; Sato, H.; Ootsuka, F. Local Mechanical-Stress Control (LMC): A New Technique for CMOS-Performance Enhancement. *IEEE International Electron Devices Meeting* **2001**, 433–436.
- (8) Armstrong, M.; Auth, C.; Ce', S.; Coan, T.; Ghani, T.; Hoffmann, T.; Murthy, A.; Sandford, J.; Shaheed, R.; Zawadzki, K.; Zhang, K.; Thompson, S.; Bohr, M. Delaying Forever: Uniaxial Strained Silicon Transistors in a 90 nm CMOS Technology. *Symposium on VLSI Technology* **2004**, 50–51.

- (9) Das, S.; Sebastian, A.; Pop, E.; McClellan, C. J.; Franklin, A. D.; Grasser, T.; Knobloch, T.; Illarionov, Y.; Penumatcha, A. V.; Appenzeller, J.; Chen, Z.; Zhu, W.; Asselberghs, I.; Li, L. J.; Avci, U. E.; Bhat, N.; Anthopoulos, T. D.; Singh, R. Transistors Based on Two-Dimensional Materials for Future Integrated Circuits. *Nat Electron* **2021**, *4*, 786–799.
- (10) Zhu, J.; Park, J. H.; Vitale, S. A.; Ge, W.; Jung, G. S.; Wang, J.; Mohamed, M.; Zhang, T.; Ashok, M.; Xue, M.; Zheng, X.; Wang, Z.; Hansryd, J.; Chandrakasan, A. P.; Kong, J.; Palacios, T. Low-Thermal-Budget Synthesis of Monolayer Molybdenum Disulfide for Silicon Back-End-of-Line Integration on a 200 mm Platform. *Nat Nanotechnol* **2023**, *18*, 456–463.
- (11) Tang, A.; Kumar, A.; Jaikissoon, M.; Saraswat, K.; Wong, H.-S. P.; Pop, E. Toward Low-Temperature Solid-Source Synthesis of Monolayer MoS₂. *ACS Appl Mater Interfaces* **2021**, *13*, 41866–41874.
- (12) McClellan, C. J.; Yalon, E.; Smithe, K. K. H.; Suryavanshi, S. V.; Pop, E. High Current Density in Monolayer MoS₂ Doped by AlO_x. *ACS Nano* **2021**, *15*, 1587–1596.
- (13) Lan, H.-Y.; Oleshko, V. P.; Davydov, A. V.; Appenzeller, J.; Chen, Z. Dielectric Interface Engineering for High-Performance Monolayer MoS₂ Transistors via TaO_x Interfacial Layer. *IEEE Trans Electron Devices* **2023**, *70* (4), 2067–2074.
- (14) Shen, P.-C.; Su, C.; Lin, Y.; Chou, A. S.; Cheng, C. C.; Park, J. H.; Chiu, M. H.; Lu, A. Y.; Tang, H. L.; Tavakoli, M. M.; Pitner, G.; Ji, X.; Cai, Z.; Mao, N.; Wang, J.; Tung, V.; Li, J.; Bokor, J.; Zettl, A.; Wu, C. I.; Palacios, T.; Li, L. J.; Kong, J. Ultralow Contact Resistance between Semimetal and Monolayer Semiconductors. *Nature* **2021**, *593*, 211–217.
- (15) Li, W.; Gong, X.; Yu, Z.; Ma, L.; Sun, W.; Gao, S.; Köroğlu, Ç.; Wang, W.; Liu, L.; Li, T.; Ning, H.; Fan, D.; Xu, Y.; Tu, X.; Xu, T.; Sun, L.; Wang, W.; Lu, J.; Ni, Z.; Li, J.; Duan, X.; Wang, P.; Nie, Y.; Qiu, H.; Shi, Y.; Pop, E.; Wang, J.; Wang, X. Approaching the Quantum Limit in Two-Dimensional Semiconductor Contacts. *Nature* **2023**, *613*, 274–279.
- (16) English, C. D.; Shine, G.; Dorgan, V. E.; Saraswat, K. C.; Pop, E. Improved Contacts to MoS₂ Transistors by Ultra-High Vacuum Metal Deposition. *Nano Lett* **2016**, *16*, 3824–3830.
- (17) Hosseini, M.; Elahi, M.; Pourfath, M.; Esseni, D. Strain-Induced Modulation of Electron Mobility in Single-Layer Transition Metal Dichalcogenides MX₂ (M = Mo, W; X = S, Se). *IEEE Trans Electron Devices* **2015**, *62*, 3192–3198.
- (18) Hosseini, M.; Elahi, M.; Pourfath, M.; Esseni, D. Strain Induced Mobility Modulation in Single-Layer MoS₂. *J Phys D Appl Phys* **2015**, *48*, 375104.
- (19) Sohler, T.; Ponomarev, E.; Gibertini, M.; Berger, H.; Marzari, N.; Ubrig, N.; Morpurgo, A. F. Enhanced Electron-Phonon Interaction in Multivalley Materials. *Phys Rev X* **2019**, *9* (3), 031019.
- (20) Peña, T.; Chowdhury, S. A.; Azizimanesh, A.; Sewaket, A.; Askari, H.; Wu, S. M. Strain Engineering 2D MoS₂ with Thin Film Stress Capping Layers. *2D Mater* **2021**, *8*, 045001.
- (21) Michail, A.; Delikoukos, N.; Parthenios, J.; Galiotis, C.; Papagelis, K. Optical Detection of Strain and Doping Inhomogeneities in Single Layer MoS₂. *Appl Phys Lett* **2016**, *108*, 173102.
- (22) Datye, I. M.; Daus, A.; Grady, R. W.; Brenner, K.; Vaziri, S.; Pop, E. Strain-Enhanced Mobility of Monolayer MoS₂. *Nano Lett* **2022**, *22*, 8052–8059.

- (23) Chai, Y.; Su, S.; Yan, D.; Ozkan, M.; Lake, R.; Ozkan, C. S. Strain Gated Bilayer Molybdenum Disulfide Field Effect Transistor with Edge Contacts. *Sci Rep* **2017**, *7*, 41593.
- (24) Kaloyeros, A. E.; Jové, F. A.; Goff, J.; Arkles, B. Review—Silicon Nitride and Silicon Nitride-Rich Thin Film Technologies: Trends in Deposition Techniques and Related Applications. *ECS Journal of Solid State Science and Technology* **2017**, *6*, 691–714.
- (25) Mackenzie, K. D.; Johnson, D. J.; Devre, M. W.; Westerman, R. J.; Reelfs, B. H. Stress Control of Si-Based PECVD Dielectrics. *Proceedings of the 207th Electrochemical Society Meeting* **2005**, 148–159.
- (26) Smithe, K. K. H.; English, C. D.; Suryavanshi, S. V.; Pop, E. Intrinsic Electrical Transport and Performance Projections of Synthetic Monolayer MoS₂ Devices. *2D Mater* **2017**, *4*, 011009.
- (27) Mignuzzi, S.; Pollard, A. J.; Bonini, N.; Brennan, B.; Gilmore, I. S.; Pimenta, M. A.; Richards, D.; Roy, D. Effect of Disorder on Raman Scattering of Single-Layer MoS₂. *Phys Rev B* **2015**, *91*, 195411.
- (28) Schauble, K.; Zakhidov, D.; Yalon, E.; Deshmukh, S.; Grady, R. W.; Cooley, K. A.; McClellan, C. J.; Vaziri, S.; Passarello, D.; Mohny, S. E.; Toney, M. F.; Sood, A. K.; Salleo, A.; Pop, E. Uncovering the Effects of Metal Contacts on Monolayer MoS₂. *ACS Nano* **2020**, *14* (11), 14798–14808.
- (29) Thompson, S. E.; Armstrong, M.; Auth, C.; Alavi, M.; Buehler, M.; Chau, R.; Cea, S.; Ghani, T.; Glass, G.; Hoffman, T.; Jan, C. H.; Kenyon, C.; Klaus, J.; Kuhn, K.; Ma, Z.; McIntyre, B.; Mistry, K.; Murthy, A.; Obradovic, B.; Nagisetty, R.; Nguyen, P.; Sivakumar, S.; Shaheed, R.; Shifren, L.; Tufts, B.; Tyagi, S.; Bohr, M.; El-Mansy, Y. A 90-Nm Logic Technology Featuring Strained-Silicon. *IEEE Trans Electron Devices* **2004**, *51*, 1790–1797.
- (30) Leonhardt, A.; Chiappe, D.; Afanas'ev, V. V.; El Kazzi, S.; Shlyakhov, I.; Conard, T.; Franquet, A.; Huyghebaert, C.; De Gendt, S. Material-Selective Doping of 2D TMDC through Al_xO_y Encapsulation. *ACS Appl Mater Interfaces* **2019**, *11*, 42697–42707.
- (31) Reboh, S.; Morin, P.; Hÿtch, M. J.; Houdellier, F.; Claverie, A. Mechanics of Silicon Nitride Thin-Film Stressors on a Transistor-like Geometry. *APL Mater* **2013**, *1*, 042117.
- (32) Thompson, S. E.; Sun, G.; Choi, Y. S.; Nishida, T. Uniaxial-Process-Induced Strained-Si: Extending the CMOS Roadmap. *IEEE Trans Electron Devices* **2006**, *53*, 1010–1020.
- (33) John, A. P.; Thenapparambil, A.; Thalakulam, M. Strain-Engineering the Schottky Barrier and Electrical Transport on MoS₂. *Nanotechnology* **2020**, *31*, 275703.
- (34) Manzanares-Negro, Y.; Quan, J.; Rassekh, M.; Moaied, M.; Li, X.; Ares, P.; Palacios, J. J.; Gomez-Herrero, J.; Gomez-Navarro, C. Low Resistance Electrical Contacts to Few-Layered MoS₂ by Local Pressurization. *2D Mater* **2023**, *10* (2), 021003.
- (35) Chen, Y.; Ke, F.; Ci, P.; Ko, C.; Park, T.; Saremi, S.; Liu, H.; Lee, Y.; Suh, J.; Martin, L. W.; Ager, J. W.; Chen, B.; Wu, J. Pressurizing Field-Effect Transistors of Few-Layer MoS₂ in a Diamond Anvil Cell. *Nano Lett* **2017**, *17* (1), 194–199.
- (36) Kaushik, N.; Nipane, A.; Basheer, F.; Dubey, S.; Grover, S.; Deshmukh, M. M.; Lodha, S. Schottky Barrier Heights for Au and Pd Contacts to MoS₂. *Appl Phys Lett* **2014**, *105*, 113505.

- (37) Lim, J. S.; Thompson, S. E.; Fossum, J. G. Comparison of Threshold-Voltage Shifts for Uniaxial and Biaxial Tensile-Stressed n-MOSFETs. *IEEE Electron Device Letters* **2004**, *25* (11), 731–733.
- (38) Hashemi, P.; Ando, T.; Cartier, E. A.; Lee, K.-L.; Bruley, J.; Lee, C.-H.; Narayanan, V. High Performance and Reliable Strained SiGe PMOS FinFETs Enabled by Advanced Gate Stack Engineering. In *2017 IEEE International Electron Devices Meeting (IEDM)*; IEEE, 2017; pp 37.3.1-37.3.4.
- (39) Cheng, Z.; Pang, C. S.; Wang, P.; Le, S. T.; Wu, Y.; Shahrjerdi, D.; Radu, I.; Lemme, M. C.; Peng, L. M.; Duan, X.; Chen, Z.; Appenzeller, J.; Koester, S. J.; Pop, E.; Franklin, A. D.; Richter, C. A. How to Report and Benchmark Emerging Field-Effect Transistors. *Nat Electron* **2022**, *5* (7), 416–423.
- (40) Late, D. J.; Liu, B.; Matte, H. S. S. R.; Dravid, V. P.; Rao, C. N. R. Hysteresis in Single-Layer MoS₂ Field Effect Transistors. *ACS Nano* **2012**, *6*, 5635–5641.

Acknowledgements

This work was performed in part at the Stanford Nanofabrication Facility (SNF) and the Stanford Nano Shared Facilities (SNSF), which are supported by the National Science Foundation (NSF) under award ECCS-2026822. This work was partly supported by the Stanford SystemX Alliance, Samsung Global Research Outreach (GRO) program, and Intel Corporation. M.J. and K.M.N acknowledge support from the Stanford Graduate Fellowship. C.K. and E.P. acknowledge the support of the ASCENT and SUPREME JUMP Centers, both Semiconductor Research Corporation (SRC) programs sponsored by DARPA. J.A.Y. acknowledges support from NSF Graduate Research Fellowship. The authors wish to thank James P. McVittie and Muyu Xue for fruitful discussions.

Author contributions

M.J., E.P. and K.C.S. conceived the work. M.J. performed the MoS₂ CVD growth, SiN_x recipe development, device fabrication, optical characterization, electrical measurement and scanning electron microscopy. C.K. contributed all numerical simulations of strain profiles. K.M.N. performed WSe₂ CVD growth, and atomic layer deposition with J.A.Y. M.J. analyzed all data and wrote the manuscript with help from C.K. and E.P. All authors have given approval to the final version of the manuscript.

Data availability

The data that support the plots within this paper and other findings of this study are available from the corresponding author upon reasonable request.

Competing financial interests

The authors declare no competing financial interests.

Supplementary Information

CMOS-compatible Strain Engineering for High-Performance Monolayer Semiconductor Transistors

Marc Jaikissoon¹, Çağıl Köroğlu¹, Jerry A. Yang¹, Kathryn M. Neilson¹, Krishna C. Saraswat^{1,2}, Eric Pop^{1,2,3,*}

¹*Department of Electrical Engineering, Stanford University, Stanford, CA 94305, U.S.A.*

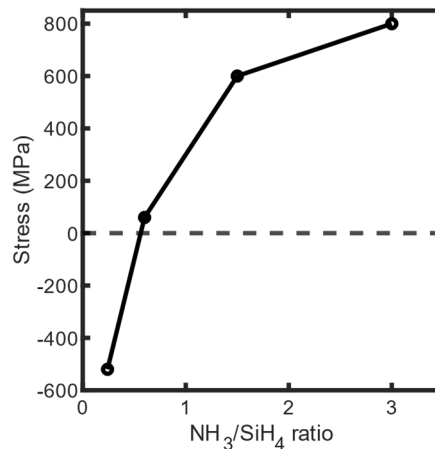
²*Department of Materials Science & Engineering, Stanford University, Stanford, CA 94305, U.S.A.*

³*Precourt Institute for Energy, Stanford University, Stanford, CA 94305, U.S.A.*

*Corresponding author email: epop@stanford.edu

1. Silicon Nitride Film Stress Measurement

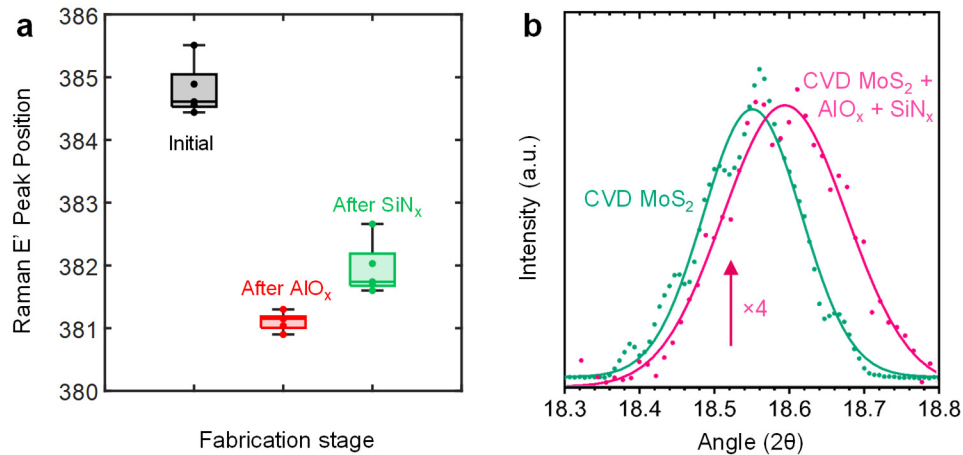
We benchmark our SiN_x deposition by measuring film stress on reference 4" silicon wafers as described in the Methods section. The Stoney equation $r = (E_s t_s^2) / [6(1 - \nu_s) \sigma_f t_f]$ was used, where r is the radius of curvature of the sample measured by laser deflection, σ_f is the desired film stress, t_f is the film thickness measured by ellipsometry, ν_s is the Poisson's ratio of the substrate, t_s is the substrate thickness and E_s is the Young's modulus of the substrate. **Supplementary Figure 1** shows the measured film stress of several SiN_x films deposited with various ratios of NH₃:SiH₄, demonstrating the tunable nature of stress from compressive (≈ -600 MPa) to tensile (≈ 800 MPa).



Supplementary Figure 1 | SiN_x stress measurement. Measured film stress in SiN_x deposited by PE-CVD at 350 °C as a function of NH₃:SiH₄ precursor ratio.

2. Raman and XRD Analysis of Strain in As-Grown and Encapsulated MoS₂ Films

We acquired Raman spectra at each stage of encapsulation, and the fitted E' peak position over several spots on the sample are summarized in **Supplementary Figure 2a**. The AlO_x capping (1.5 nm Al seed + 10 nm Al₂O₃ by ALD) causes a large, nearly $\approx 4 \text{ cm}^{-1}$, redshift of the E' peak of MoS₂. This would appear to imply a tensile strain $> 1.5\%$, however we have found in previous work¹ that Raman analysis greatly overestimates MoS₂ strain under such encapsulation (as compared to X-ray diffraction measurements). The apparent shift of the E' peak is instead caused by doping and plasmon coupling of the MoS₂ with the encapsulation layer.¹ This renders Raman analysis unreliable for quantifying MoS₂ strain under such encapsulation layers. We also note that the Raman spot size ($\sim 0.5 \mu\text{m}$) makes probing of nanoscale strain distributions difficult, especially in our 200 nm devices.

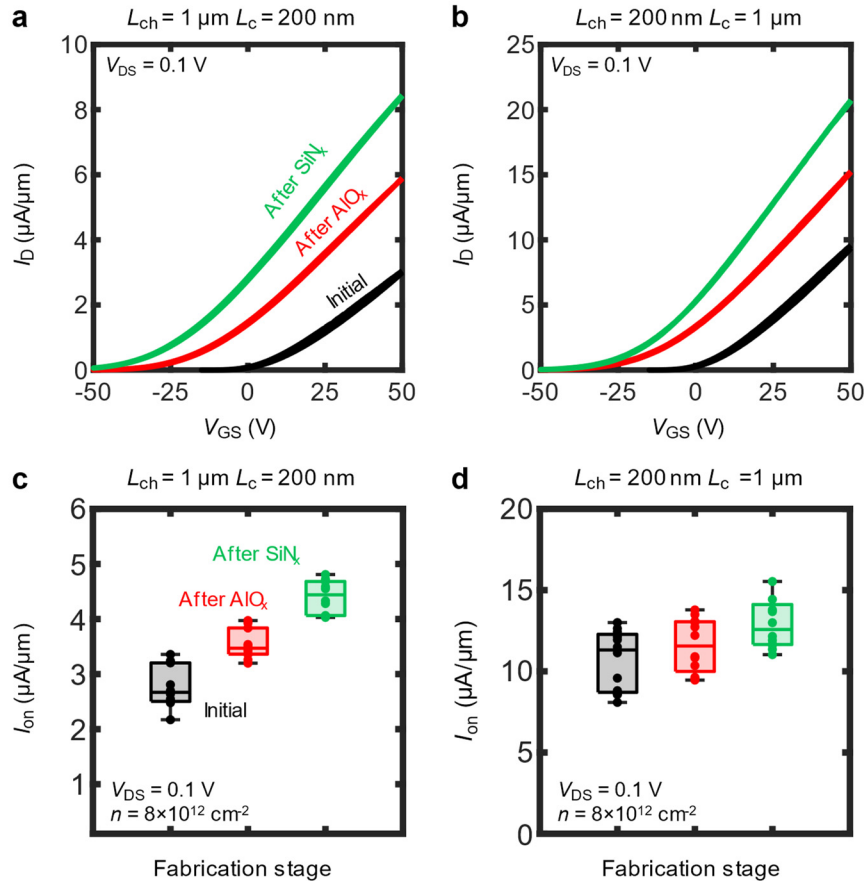


Supplementary Figure 2 | Raman vs. Grazing Incidence X-Ray Diffraction for Quantifying Strain. **a**, Raman E' peak position acquired at several spots on unpatterned, as-grown MoS₂ (on SiO₂) before and after encapsulation with AlO_x and SiN_x. **b**, Grazing-incidence X-ray diffraction spectra acquired on as-grown MoS₂ before and after capping with AlO_x and high-tensile stress SiN_x.

To accurately probe strain in MoS₂ films, we used grazing incidence X-ray diffraction measurements with a synchrotron X-ray source on as-grown MoS₂, before and after capping with AlO_x and high-tensile stress SiN_x, as shown in **Supplementary Figure 2b**. We observe an increase of 0.0422° of the in-plane (10) peak position of MoS₂, corresponding to a compressive biaxial strain of -0.23% after capping. (The tensile SiN_x contracts to relieve its built-in stress, in the process compressing the MoS₂ underneath.) However, the large X-ray spot size (several mm) also makes precise strain mapping difficult, therefore we used finite element simulations (main text **Figure 3** and **Supplementary Information Sections 5-7**) to provide insight into the strain profiles and distributions in capped MoS₂, particularly within our nanoscale transistors (where strain is uniaxial, due to the presence of contacts).

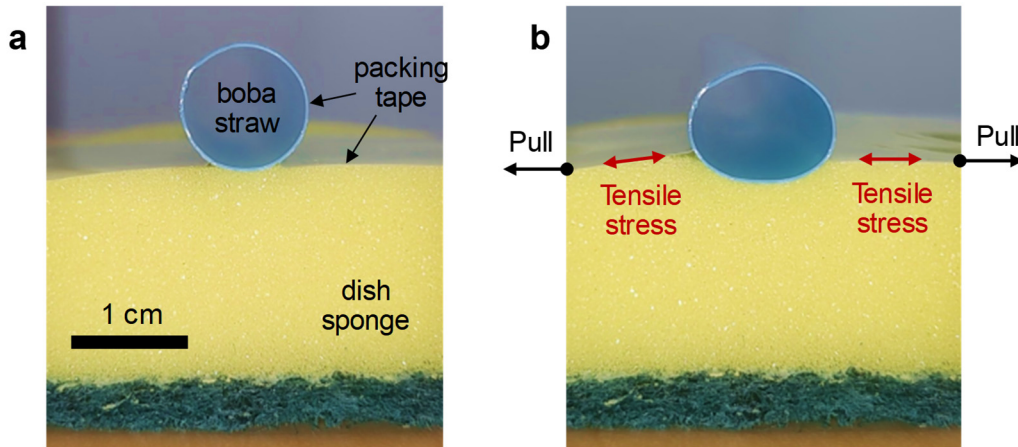
3. Other Back-gated Channel and Contact Combinations

In addition to using ‘long’ and ‘short’ geometries (channel and contact length $L_{\text{ch}} = L_{\text{c}} = 1 \mu\text{m}$ and 200 nm , respectively) mentioned in the main text, we also tested other combinations of L_{ch} and L_{c} . The drain current vs. gate voltage ($I_{\text{D}}-V_{\text{GS}}$) of devices with $L_{\text{ch}} = 1 \mu\text{m}$, $L_{\text{c}} = 200 \text{ nm}$ and $L_{\text{ch}} = 200 \text{ nm}$, $L_{\text{c}} = 1 \mu\text{m}$ are shown in **Supplementary Figure 3a,b**. Both cases demonstrate negative threshold voltage (V_{T}) shifts as reported for the devices in the main text after AlO_x and SiN_x capping, as well as improvements to transconductance ($g_{\text{m}} = \partial I_{\text{D}}/\partial V_{\text{GS}}$). Normalizing by carrier density to account for V_{T} shifts, box plots of I_{on} extracted at a carrier density of $n \approx 8 \times 10^{12} \text{ cm}^{-2}$ are shown for $L_{\text{ch}} = 1 \mu\text{m}$, $L_{\text{c}} = 200 \text{ nm}$ and $L_{\text{ch}} = 200 \text{ nm}$, $L_{\text{c}} = 1 \mu\text{m}$ in **Supplementary Figure 3c,d**. We observe that I_{on} only increases by up to 27% for these combinations, indicating that larger improvements are only possible when both L_{ch} and L_{c} are reduced, as in the main text.



Supplementary Figure 3 | Characterization of other back-gated transistor geometries. Back-gated transfer characteristics of high-stress SiN_x -capped MoS_2 transistor with **a**, $L_{\text{ch}} = 1 \mu\text{m}$, $L_{\text{c}} = 200 \text{ nm}$ and **b**, $L_{\text{ch}} = 200 \text{ nm}$, $L_{\text{c}} = 1 \mu\text{m}$. Box plots of normalized on-state current (I_{on}) at $n = 8 \times 10^{12} \text{ cm}^{-2}$ for several devices, after each fabrication step. **c**, $L_{\text{ch}} = 1 \mu\text{m}$, $L_{\text{c}} = 200 \text{ nm}$ and **d**, $L_{\text{ch}} = 200 \text{ nm}$, $L_{\text{c}} = 1 \mu\text{m}$. All measurements are carried out at room temperature and $V_{\text{DS}} = 0.1 \text{ V}$.

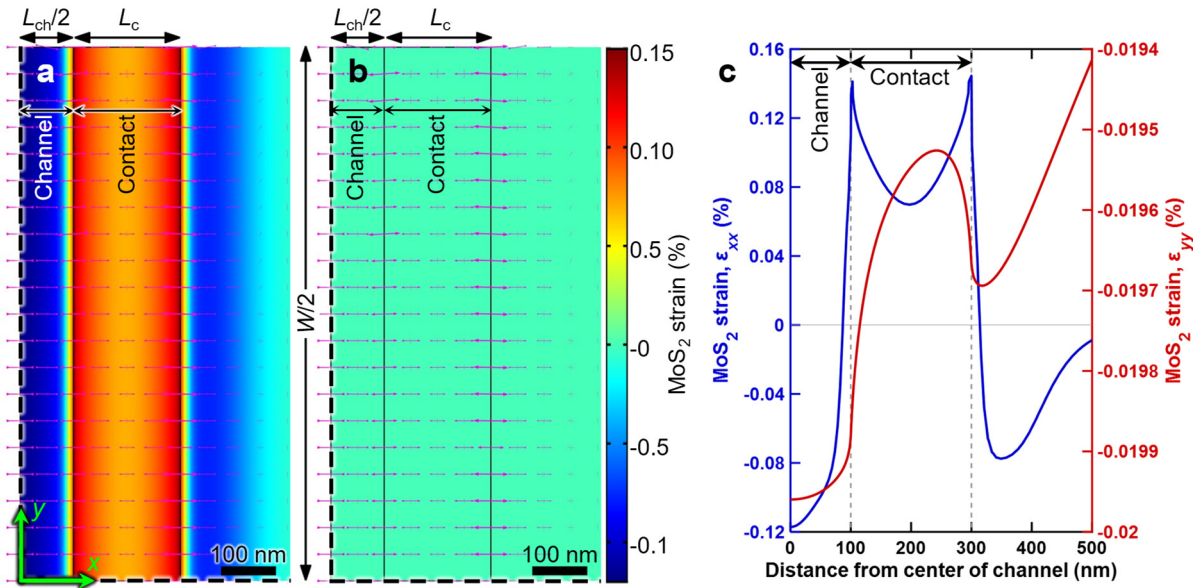
4. Macroscopic Visual Model of Deformation due to Tensile-Stressed Capping Layer



Supplementary Figure 4 | Visualization of contact electrode deformation using everyday objects. **a**, The cross-section of a simple macroscopic visual analogy for the contact geometry of a back-gated MoS₂ transistor. Here, a plastic straw (from boba tea) stands in for the contact electrode, a dish sponge for the materials under the electrode (MoS₂/SiO₂/Si), and a piece of transparent packing tape (covering the top of the sponge and wrapping as an “Ω” around the straw) for the SiN_x film, initially unstressed. **b**, Contact deformation visualized when the duct tape is laterally tensile-stressed by pulling the tape outward from the sides, similar to the exaggerated simulated device deformation shown in **Figure 3b** of the main text.

5. Stress Simulations: Additional Information

Two-dimensional (2D) and three-dimensional (3D) stress simulations were performed for back-gated (BG) and dual-gated (DG) transistors, assuming linear elasticity. We confirmed through 3D simulations that the MoS₂ strain in the transistor width direction is small (i.e. MoS₂ strain is essentially uniaxial), as illustrated by **Supplementary Figure 5**. Consequently, 2D simulations are sufficient to accurately capture the uniaxial stress and strain distributions in our devices, and the results presented in this work were obtained through 2D simulations. After multi-scale simulations of the entire sample (including the transistor and the entire silicon substrate) confirmed that strains due to substrate bowing were negligible, later simulations used a smaller domain around the BG transistor with a fixed boundary condition at the bottom of a thinner section of substrate, with no appreciable errors in stress and strain distributions.



Supplementary Figure 5 | In-plane strain distribution across the device. **a, b**, The distributions of lengthwise in-plane strain (ϵ_{xx} given in **a**) and widthwise in-plane strain (ϵ_{yy} given in **b**) in MoS₂ in a BG transistor (with 600 MPa tensile-stressed SiN_x capping) for $L_{ch} = L_c = 200$ nm, as viewed from above. The bottom left corner corresponds to the center of the device, with the dashed lines indicating the two symmetry planes. The magenta arrows indicate the principal strain directions and values at each point, showing that the strain is predominantly in the direction of current flow (i.e. along the x -axis), and hence uniaxial. **c**, MoS₂ strains ϵ_{xx} (left axis) and ϵ_{yy} (right axis) along positive x -axis of the same device showing the widthwise strain is small, with a nearly uniform compressive strain $< 0.02\%$ in magnitude.

An isotropic “initial stress” (the stress before the geometry is allowed to relax) of 600 MPa was assumed in the SiN_x capping layer. The isotropic elastic properties assumed for the materials other than

MoS₂ are summarized in **Supplementary Table 1**. In contrast, MoS₂ is only transversely isotropic (i.e. isotropic in-plane), and thus is described by an anisotropic stiffness tensor. The elastic properties were taken from Li *et al.*², and can be summarized as $E_{xx} = E_{yy} = 265$ GPa, $E_{zz} = 100$ GPa, $G_{xz} = G_{yz} = 50$ GPa, and $\nu_{xy} = \nu_{yx} = \nu_{xz} = \nu_{yz} = 0.25$. Here, x and y correspond to the in-plane directions and z to the cross-plane direction, E denotes Young’s modulus, G denotes shear modulus and ν_{ij} denotes Poisson’s ratio for loading along i and transverse direction j . The remaining elastic properties can be determined from these, e.g. $\nu_{zx} = (E_{zz}/E_{xx})\nu_{xz}$ and $G_{xy} = E_{xx}/[2(1 + \nu_{xy})]$.

Supplementary Table 1: Young’s moduli and Poisson’s ratios assumed for materials except for MoS₂.

	Si	SiO ₂	AlO _x	SiN _x	Au	Pd
Young’s modulus (GPa)	170	70	400	250	70	73
Poisson’s ratio	0.28	0.17	0.22	0.23	0.44	0.44

The MoS₂ grown by CVD (at 750 °C) directly on SiO₂ is tensile-stressed, which has been attributed to the mismatch in coefficients of thermal expansion^{3–5} α_{MoS_2} and α_{SiO_2} . To model this observation, we take $\alpha_{\text{MoS}_2} = 7 \times 10^{-6} \text{ K}^{-1}$ and $\alpha_{\text{SiO}_2} = 2 \times 10^{-6} \text{ K}^{-1}$, yielding an initial thermally-induced strain of $(\alpha_{\text{MoS}_2} - \alpha_{\text{SiO}_2})(T_{\text{growth}} - T_{\text{ambient}}) \cong 0.37\%$ in MoS₂, which represents the tensile strain in a planar MoS₂ film as-grown, relative to relaxed MoS₂. The in-plane strains reported in this work are all relative to MoS₂ as-grown: the residual MoS₂ strain (assumed 0.37% here) should be added to these values to obtain strains relative to relaxed MoS₂. We note that the built-in tensile stress in MoS₂ has negligible effect on the in-plane strains in MoS₂ in the relaxed structure, because MoS₂ is so thin and its film force (stress times thickness) is small compared to that effected by the stress in SiN_x. In other words, the MoS₂ strain is dictated mainly by the adjacent materials, and ultimately caused by the tensile stress in SiN_x.

We also note that it is possible for there to be some amount of slipping between MoS₂ and adjacent materials due to poor adhesion. While the quantitative details of this process are scarce and slipping is not included in the results we present, if MoS₂ is allowed to slip freely on the underlying SiO₂, simulations predict that the strains in both the channel and under the contacts increase by up to ~50%, and the strain peaks near the contact edges become more “rounded.” However, the trends in the main text and **Supplementary Information Section 6** otherwise stay the same.

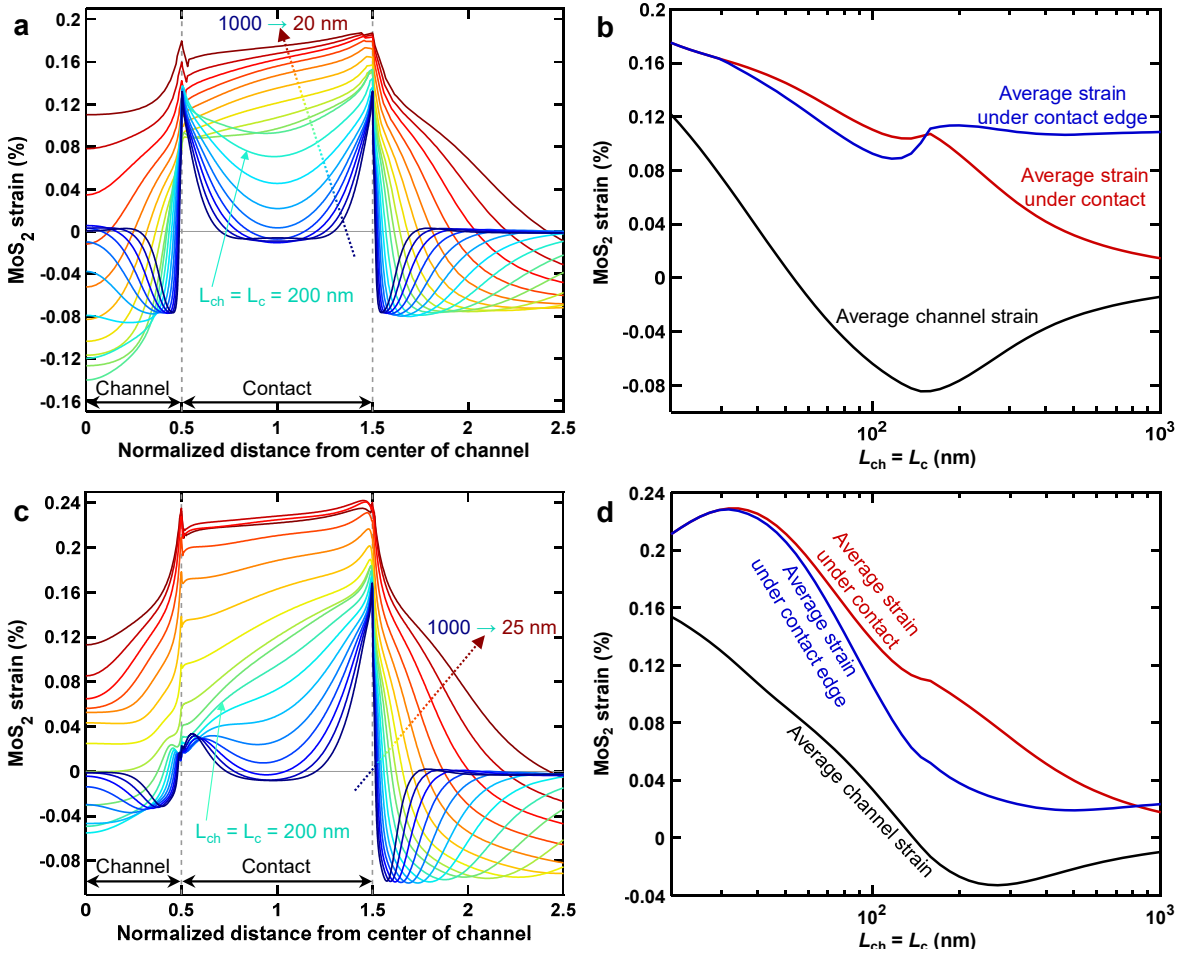
We note that all strain simulations in the subsequent sections assume a tensile-stressed SiN_x capping layer (600 MPa, as measured in our experiments) on top of either a DG or BG transistor geometry.

6. Strain Projections for Channel and Contact Scaling

We carried out additional simulations to study the impact of the SiN_x stressor on MoS₂ strain distributions in BG and DG transistors with different channel and contact lengths. Because our DG transistor geometry is similar to that of a typical top-gated (TG) transistor except for the conductive substrate, the corresponding conclusions apply equally well to TG devices (with no BG). The metrics we focus on are the average channel strain (in-plane, along the channel direction), average strain in MoS₂ under the contacts, and MoS₂ under the edge of the contact. The latter parameter is quantified as the average strain in the first 30 nm (or L_c , whichever is smaller) of MoS₂ under the contact, on the channel side. This parameter is relevant because the current under a contact is only distributed within about a few transfer lengths L_T of the contact edge, which is typically^{6,7} on the order of tens of nanometers in good contacts with MoS₂.

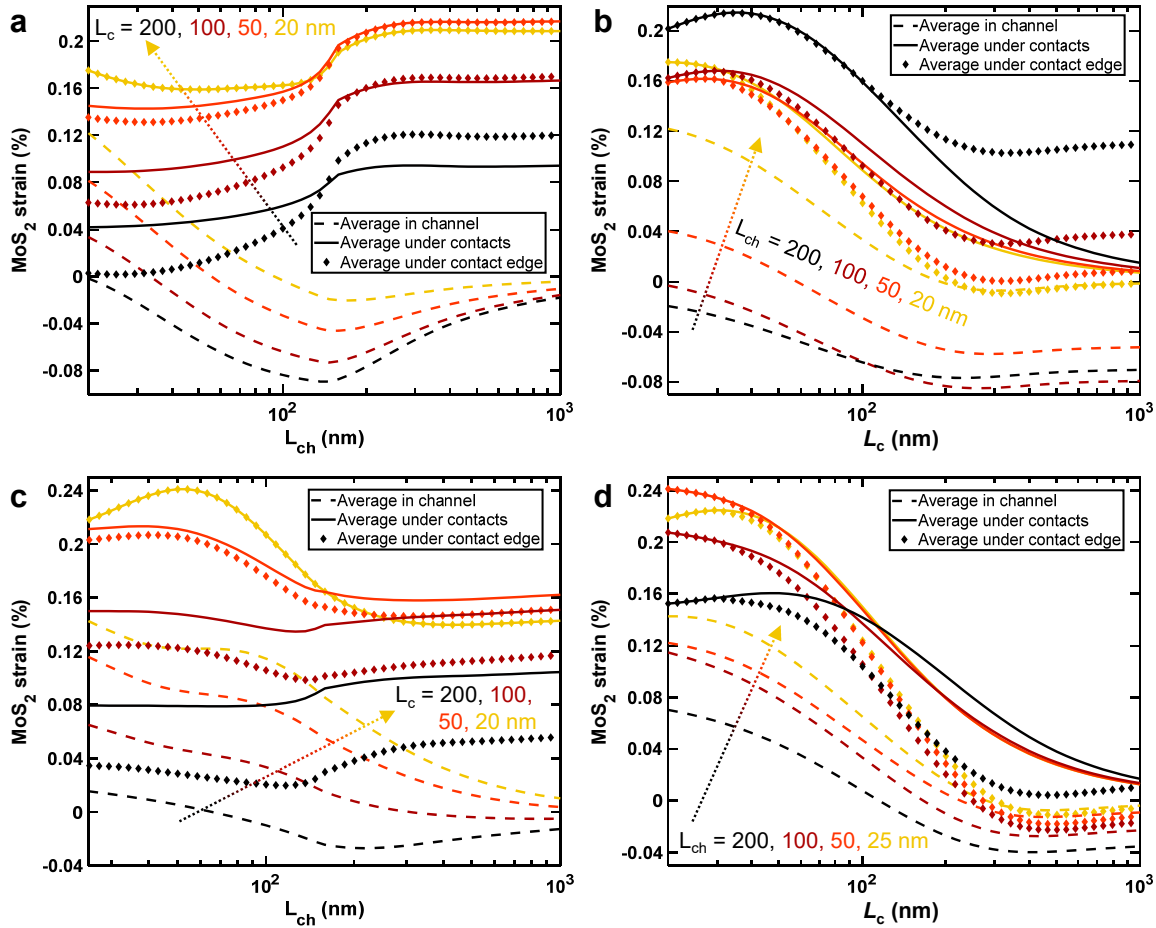
Supplementary Figure 6 shows the variation of the in-plane strain as a function of $L_{ch} = L_c$, for the BG (**Supplementary Figure 6a,b**) and DG (**Supplementary Figure 6c,d**) devices. **Supplementary Figure 6a** shows that in a BG transistor, the strain under contact is highest and approximately equal at the two edges. However, according to **Supplementary Figure 6c**, a DG transistor has lower strain under the “inner” contact edge than under the “outer” edge. This is because the nitride stressor only directly covers the outer side of the contacts in the DG device and not both sides like it does in the BG geometry. Consequently, as can be seen in **Supplementary Figure 6b,d**, the DG transistor has lower average tensile strain under the contacts for $L_{ch} > 100$ nm, but in shorter devices the DG transistor has higher tensile strain under the contacts as well as in the channel. Reducing the channel and contact lengths toward 20 nm in both BG and DG transistors increases the tensile strain under the contacts substantially, suggesting further improvements of contact resistance (with strain) are possible. Moreover, the tensile-strained channel at shorter channel lengths could lead to increased mobility^{8,9}, and thus, further performance enhancement. The kink seen in **Supplementary Figure 6b,d** at $L_{ch} = 160$ nm is the result of the fact that for $L_{ch} < 160$ nm, the curved sections of the nitride film above the channel, where it smoothly conforms around the edges of the contact (in the BG device) or the top gate (in the DG device), begin to merge.

We also varied L_{ch} and L_c separately to study their individual effects on the strain distribution in MoS₂, the results are given in **Supplementary Figure 7**. According to **Supplementary Figure 7a**, reducing L_{ch} below 160 nm in a BG transistor reduces the tensile strain under the contacts, especially for long contacts. This happens because in the limit of very short channels, the contacts effectively “merge”,



Supplementary Figure 6 | Stress simulations and projections. **a**, The strain profiles along MoS₂ in a BG transistor (with 600 MPa tensile-stressed SiN_x capping), normalized by L_{ch} , for $L_{ch} = L_c$ varied from 1000 nm down to 20 nm (logarithmically spaced). **b**, The corresponding average in-plane strains along MoS₂ as a function of $L_{ch} = L_c$. **c**, The normalized strain profiles along MoS₂ in a DG transistor, for $L_{ch} = L_c$ varied from 1000 nm down to 25 nm (logarithmically spaced). **d**, Average in-plane strains in MoS₂ in a DG transistor, as a function of $L_{ch} = L_c$. **e**, The corresponding average in-plane strains along MoS₂ as a function of $L_{ch} = L_c$.

and the strain under the inner contact edge is lower for the same reason the strain in under the middle of the contact is lower than at the edges. Reducing L_{ch} also increases the channel strain significantly, turning it tensile for L_{ch} close to 20 nm. According to **Supplementary Figure 7b**, reducing L_c has a similar effect on the BG transistor channel strain, and also increases both the edge and average contact strains as it is reduced beyond 160 nm. **Supplementary Figure 7c** shows that in a DG transistor, reducing L_{ch} similarly increases the tensile channel strain, although its effect on contact strain is less pronounced than in the BG case. Finally, a comparison of **Supplementary Figure 7d** to



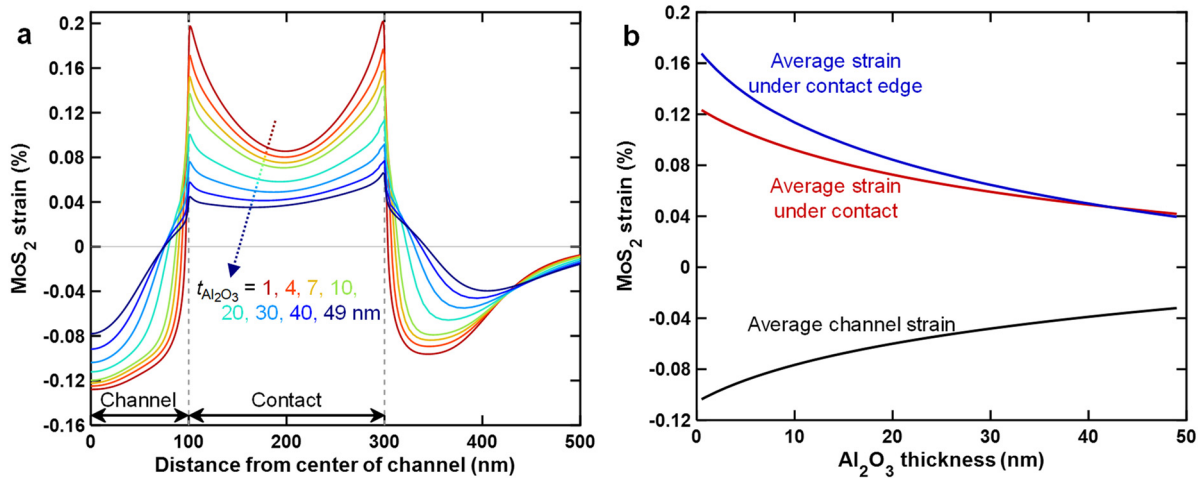
Supplementary Figure 7 | Strain projections for channel and contact scaling. Average in-plane strains in a back-gated (BG) MoS₂ transistor with a tensile-stressed SiN_x capping layer (600 MPa) when **a**, L_{ch} is varied with L_c fixed, and **b**, L_c is varied with L_{ch} fixed. Average in-plane strains in MoS₂ in a DG transistor when **c**, L_{ch} is varied with L_c fixed, and **d**, L_c is varied with L_{ch} fixed.

Supplementary Figure 7b reveals that the effect of reducing DG transistor contact lengths is similar to the BG transistor, increasing strain both in the channel and under contacts.

To summarize, in both BG and DG (or TG) transistors, shorter channels are expected to put tensile strain on the channel, while shorter contacts increase the tensile strain under the contacts as well as in the channel. Both of these effects are expected to increase performance in smaller devices, due to tensile strain under the contacts reducing contact resistance¹⁰, and tensile strain in the channel increasing mobility^{8,9}.

7. Impact of Al₂O₃ Barrier Thickness on Strain Distribution

We have carried out simulations to understand the effect of the Al₂O₃ barrier layer thickness on the strain distribution in the BG transistor, presented in **Supplementary Figure 8**. It is seen that the MoS₂ strain in both the channel and the contact regions decrease steadily as Al₂O₃ is made thicker. As such, to further improve contact resistance via strain, there is possibility of enhancing the strain under contact edges by up to 50% by making the Al₂O₃ thinner than what we have used in this work (10 nm), or possibly even eliminating it.



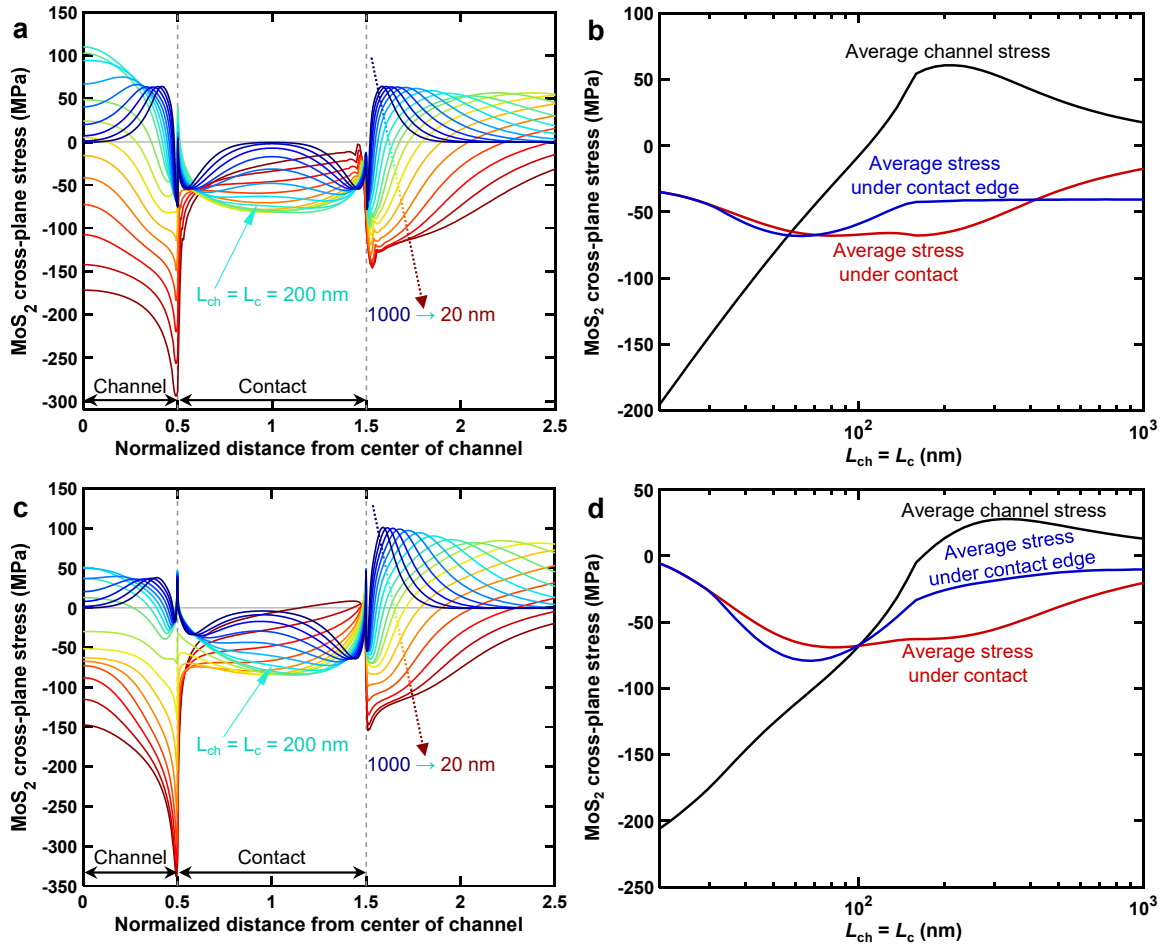
Supplementary Figure 8 | Dependence of strain profile on Al₂O₃ barrier layer thickness. a, In-plane strain distributions in a BG transistor with $L_{ch} = L_c = 200$ nm for several Al₂O₃ thicknesses ($t_{Al_2O_3}$). **b,** Average in-plane strains in MoS₂ in a BG transistor (with 600 MPa tensile-stressed SiN_x capping) as a function of Al₂O₃ thickness. The blue curve corresponds to the average strain in the first 30 nm of MoS₂ (a typical contact transfer length) under the contacts.

8. Cross-Plane Stress in MoS₂ due to “Downward Pressure” on Contacts

The tensile-stressed SiN_x capping layer pushes down on the contacts due to its tendency to contract, as visualized in **Figure 3a,b** of the main text, as well as **Supplementary Figure 4**, which may reduce the thickness of the van der Waals gap (an electron tunneling barrier) between the Au contacts and MoS₂. It is then possible that the vertical contact-MoS₂ pressure (i.e. the cross-plane MoS₂ stress) due to this effect (in addition to the in-plane tensile strain of MoS₂ under the contacts) contributes to the contact resistance improvement we observe in SiN_x-capped devices, as the reduction in MoS₂ contact resistance with applied pressure has been observed experimentally^{11,12}.

To better understand the role of the SiN_x in vertically compressing the contacts, we plot the cross-plane stress in BG (**Supplementary Figure 9a,b**) and DG (**Supplementary Figure 9c,d**) MoS₂ devices, as a function of $L_{ch} = L_c$ from 1000 nm down to ~20 nm. For both BG and DG devices, the compressive cross-plane stress at the contact is close to about 50 MPa for $50 \text{ nm} < L_{ch} = L_c < 200 \text{ nm}$. Based on measurements of Chen *et al.*¹¹ this would correspond to a contact resistance reduction of ~12%.

Another interesting feature observed in **Supplementary Figure 9b,d** is that while the vertical stress in the channel is moderately tensile for $L_{ch} = L_c > \sim 100 \text{ nm}$, scaling the devices down to $L_{ch} = L_c \sim 20 \text{ nm}$ results in a sizable compressive vertical channel stress, up to ~200 MPa. In other words, the MoS₂ channel is “vertically squeezed” by the contacts at the shortest channel and contact dimensions (here ~20 nm). This vertical compression of MoS₂ has a similar effect on the conduction band structure as lateral tensile strain¹³, i.e. lowering the K valley and raising the Q valley (thus expected to reduce intervalley scattering and improve mobility^{8,9}), and has also been reported experimentally to improve in-plane conduction¹¹. Therefore, the vertical compression of the MoS₂ channel could enable further enhancement of device performance at the smallest dimensions, in addition to the effect of in-plane tensile strain discussed in **Supplementary Information Section 6**.



Supplementary Figure 9 | Cross-plane stress in MoS₂. **a**, Normalized cross-plane stress profiles along MoS₂ in back-gated (BG) transistors (with 600 MPa tensile-stressed SiN_x capping), normalized by L_{ch} , for $L_{ch} = L_c$ from 1000 nm down to 20 nm (logarithmically spaced). **b**, Corresponding average cross-plane stresses along BG MoS₂ as a function of $L_{ch} = L_c$. “Average stress under contact edge” refers to the cross-plane stress *averaged* along the first 30 nm of contact length (30 nm is a typical value of contact transfer length). **c**, Normalized cross-plane stress profiles along MoS₂ in dual-gated (DG) transistors, for $L_{ch} = L_c$ from 1000 nm down to 20 nm (logarithmically spaced). **d**, Corresponding average cross-plane stresses in MoS₂ in DG transistors, as a function of $L_{ch} = L_c$.

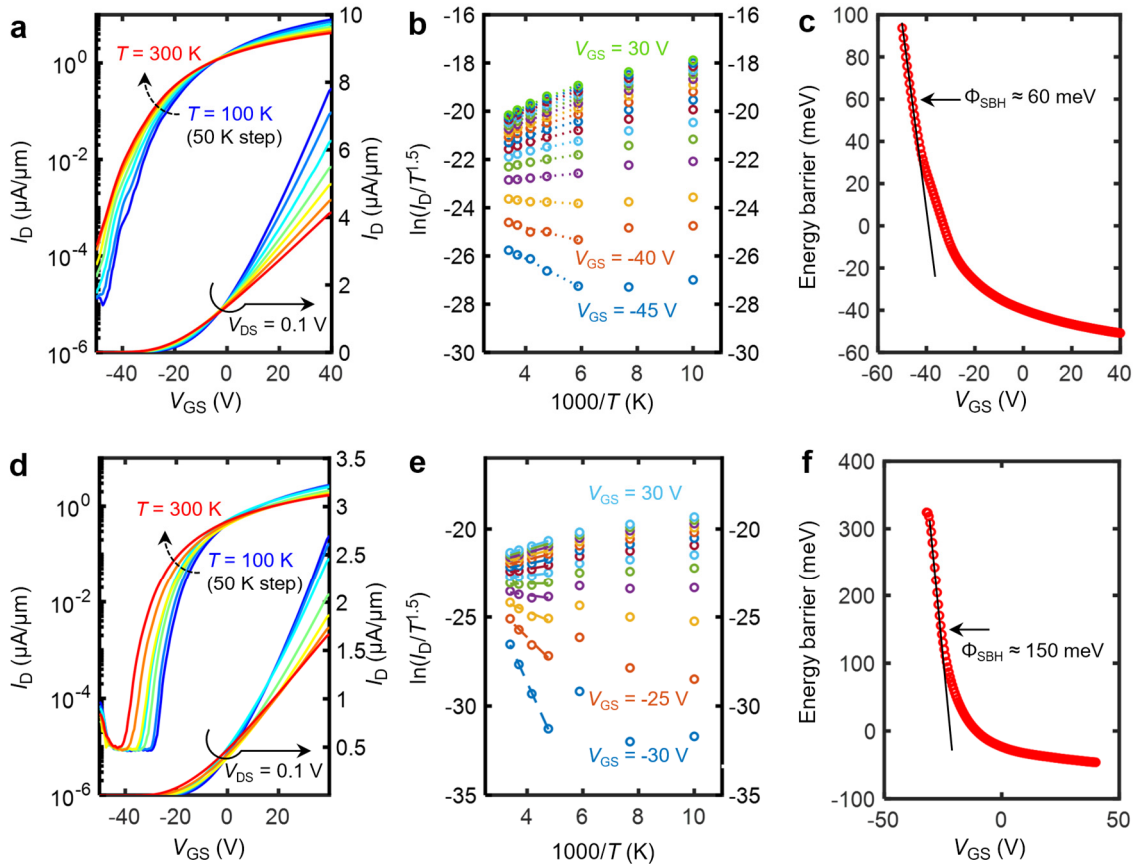
9. Schottky Barrier Height Measurement

To further investigate the behavior at the contacts, we estimate the Schottky barrier height (SBH) based on the thermionic emission current dictated by the equation:

$$I_D = A_{2D}^* T^{3/2} \exp\left(-\frac{q\Phi_{SBH}}{k_B T}\right) \left[1 - \exp\left(-\frac{qV}{k_B T}\right)\right],$$

where A_{2D}^* is the 2D-equivalent Richardson constant, T is the temperature, q is the elementary charge, k_B is Boltzmann's constant, V is the applied voltage, and Φ_{SBH} is the Schottky barrier height^{14,15}.

Supplementary Figure 10a-c shows the results of temperature-dependent measurements to extract the SBH of a strained device having $L_{ch} = 1 \mu\text{m}$ and $L_c = 200 \text{ nm}$ at $V_{DS} = 0.1 \text{ V}$, while **Supplementary Figure 10d-f** shows the results of measurements performed on an uncapped control sample with Au contacts having $L_{ch} = 2 \mu\text{m}$ and $L_c = 200 \text{ nm}$.



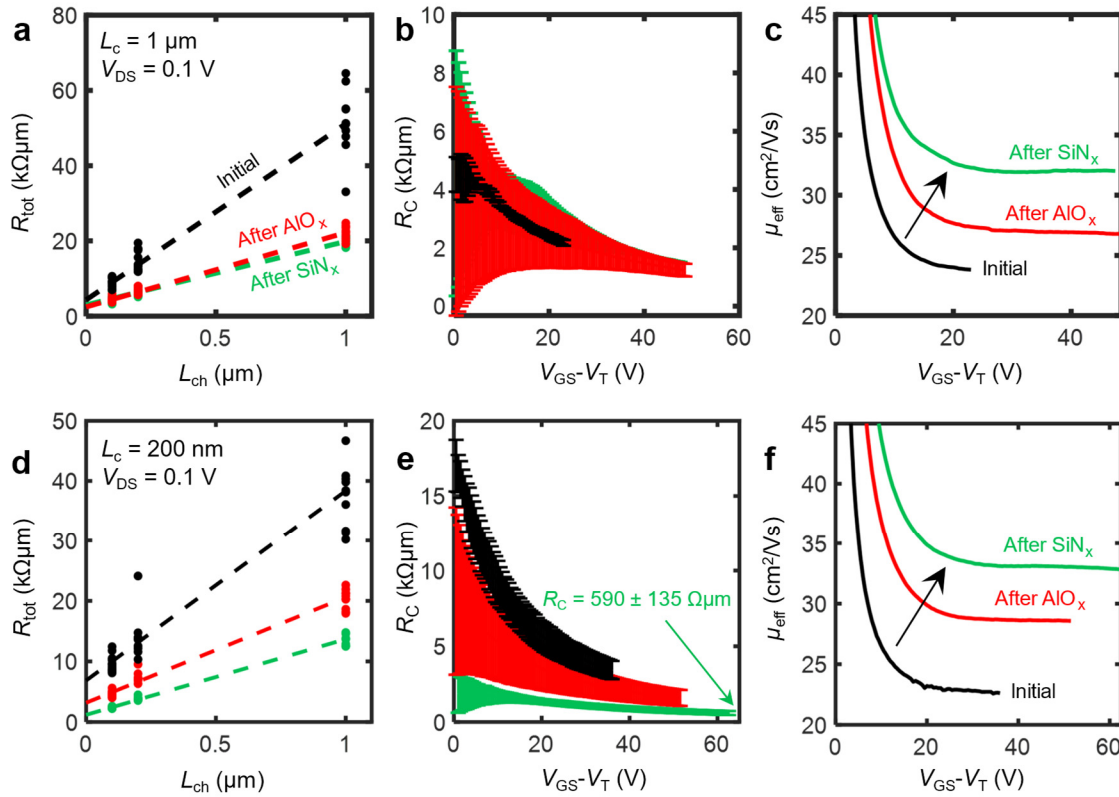
Supplementary Figure 10 | Schottky barrier height extraction. Measurements, **a-c**, (top row) of a high tensile-stress SiN_x -capped device and **d-f**, (bottom row) an uncapped control device with Au contacts. **a, d**, Temperature-dependent transfer characteristics measured between $T = 100$ and 300 K at $V_{DS} = 0.1 \text{ V}$. **b, e**, Arrhenius plots measured at various gate voltages. **c, f**, Estimates of the effective electron Schottky barrier height.

Supplementary Figure 10a shows the device I_D - V_{GS} characteristics measured from $T = 100$ to 300 K. From this, the slope of the Arrhenius plot of $\ln(I_D/T^{3/2})$ vs $1000/T$ can be constructed at each value of V_{GS} , with the slope giving the effective barrier height at that particular bias as shown in **Supplementary Figure 10b**. Finally, the estimated energy barrier is plotted vs. V_{GS} in **Supplementary Figure 10c**, with the true value of Schottky barrier height (SBH) being determined as the effective barrier height at the flat band voltage indicated by the point above which the effective barrier height starts to deviate from a linear dependence of the gate voltage. We extract a SBH of ~ 60 meV for the stressed device. The results of SBH measurement on a control device (without SiN_x capping, but otherwise identical) are shown in **Supplementary Figure 10d-f**, indicating a barrier of ~ 150 meV.

10. Pseudo-Transfer Length Method Analysis

We estimate contact resistance (R_C) and effective electron mobility (μ_{eff}) using pseudo-transfer length method^{16–18} (TLM) measurements. We call these “pseudo” TLM measurements, because we fit the median resistance (R_{tot}) vs. channel length (L_{ch}) for *all* devices we have, rather than choosing a single TLM structure⁶ with shared contacts and a larger range of L_{ch} , fabricated in a single region of MoS₂.

Supplementary Figure 11a displays $R_{\text{tot}} = L_{\text{ch}}R_{\text{sh}} + 2R_C$ vs. L_{ch} , where R_{sh} is the channel sheet resistance, for devices with ‘long’ contacts ($L_c = 1 \mu\text{m}$) at various stages of capping. To account for threshold voltage (V_T) variation, we normalize all devices to the same maximum gate overdrive ($V_{\text{ov}} = V_{\text{GS}} - V_T$) using linear extrapolation to estimate V_T . The y -intercept of the linear fit allows us to extract $2R_C$, which is plotted vs. overdrive voltage in **Supplementary Figure 11b**. For devices with ‘long’ contacts, the extracted R_C remains similar at different stages of capping. This reflects the lower average stress across the devices with long contacts. Additionally, the slope of the fit allows us to estimate the



Supplementary Figure 11 | Pseudo-transfer length method (TLM) analysis. Comparison of high tensile-stress SiN_x-capped devices fabricated with (a-c) long, 1 μm and (d-f) short, 200 nm contacts. **a, d**, R_{tot} vs. L_{ch} at maximum gate overdrive ($V_{\text{GS}} - V_T$) for $V_{\text{DS}} = 0.1 \text{ V}$, at different stages of capping. **b, e**, Extracted R_C vs. gate overdrive voltage. We observe reduced R_C after SiN_x capping only for the short contacts. **c, f**, Estimated effective mobility μ_{eff} vs. gate overdrive voltage.

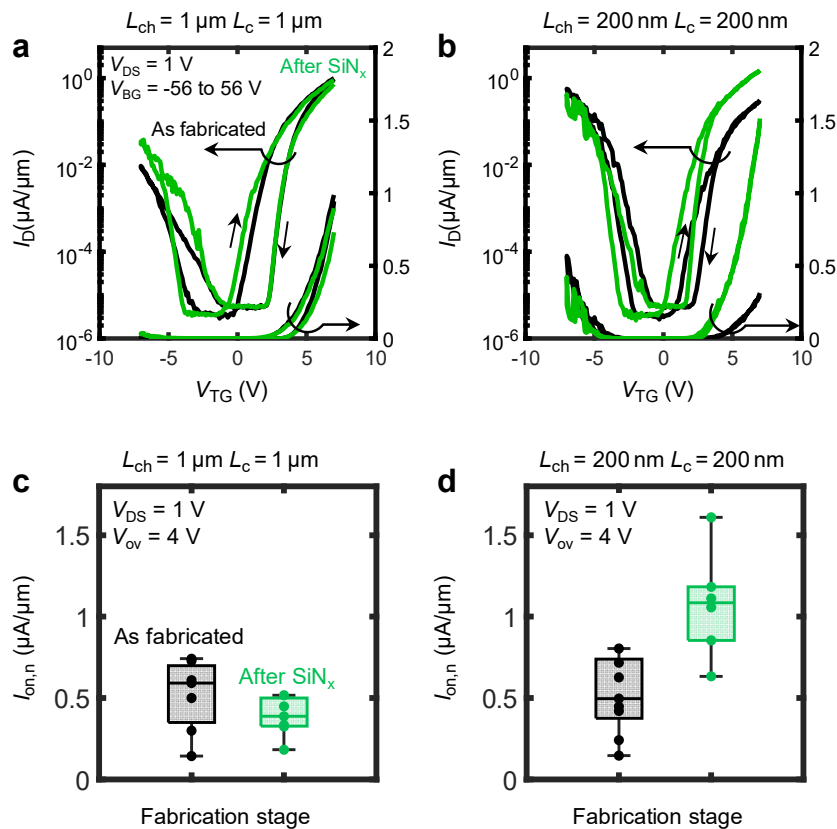
effective mobility, $\mu_{\text{eff}} = (qnR_{\text{sh}})^{-1}$ where q is the elementary charge and $n = C_{\text{ox}}(V_{\text{GS}} - V_{\text{T}} - V_{\text{DS}}/2)/q$ is the electron concentration per unit area. **Supplementary Figure 11c** shows the extracted μ_{eff} vs. overdrive voltage for devices with ‘long’ contacts, indicating a small improvement after SiN_x capping. We caution against relying too strongly on TLM mobility estimates, because the strain distribution (between the various channel lengths in the TLM) is non-uniform. In addition, we cannot be certain that the apparent mobility increase is entirely due to strain; other contributions could come from dielectric screening and the additional thermal annealing seen by the AlO_x/SiN_x capped samples. For these reasons we have put more emphasis on changes in transistor current density (I_{D}) in the main text. The current density (at a given voltage, e.g. 1 V) is also ultimately what impacts the circuit performance of a transistor.

We repeat this analysis for devices with ‘short’ contacts ($L_{\text{c}} = 200$ nm) in **Supplementary Figure 11d**. After SiN_x capping, the extracted R_{c} is now significantly reduced to $590 \pm 135 \Omega \cdot \mu\text{m}$ as shown in **Supplementary Figure 11e**, demonstrating that high-stress capping has a larger effect on the shorter contacts. The extracted mobility trend is similar in **Supplementary Figure 11f**, which is expected because the channel dimensions used are consistent with those in **Supplementary Figure 11a-c**.

11. Strained Dual-Gated WSe₂ Transistors

Monolayer WSe₂ is another TMD which is predicted to benefit from the application of uniaxial tensile strain. To further verify the effectiveness of our strain technique, we fabricated dual-gated (DG) transistors using CVD-grown monolayer WSe₂ using the approach described in the main text, with the only process difference being the use of 10 nm HfO_x deposited by atomic layer deposition at 200 °C serving as the top gate dielectric, instead of 10 nm AlO_x. The I_D - V_{GS} of DG WSe₂ transistors measured before and after capping with high tensile-stressed SiN_x are shown for ‘long’ ($L_{ch} = L_c = 1 \mu\text{m}$) and ‘short’ ($L_{ch} = L_c = 200 \text{ nm}$) devices in **Supplementary Figure 12a,b**, respectively.

We compare the n -branch I_{on} (at fixed $V_{ov} = V_{TG} - V_T > 0$) of each case in **Supplementary Figure 12c,d**. Similar to the trends observed in the case of monolayer MoS₂ (main text **Figure 4c,e**), the larger improvement of I_{on} is observed for the devices with the shortest channel and contact lengths.



Supplementary Figure 12 | Strained DG WSe₂ transistors. Dual-gated transfer characteristics of high-stress SiN_x-capped WSe₂ transistor with **a**, ‘long’ ($L_{ch} = L_c = 1 \mu\text{m}$) and **b**, ‘short’ ($L_{ch} = L_c = 200 \text{ nm}$) dimensions. Small arrows mark forward and backward sweeps. Relative improvement in n -branch I_{on} at fixed overdrive after capping with high-stress SiN_x films (green) for **c**, ‘long’ and **d**, ‘short’ devices. All measurements are carried out at room temperature and $V_{DS} = 1 \text{ V}$.

Supplementary References

- (1) Schauble, K.; Zakhidov, D.; Yalon, E.; Deshmukh, S.; Grady, R. W.; Cooley, K. A.; McClellan, C. J.; Vaziri, S.; Passarello, D.; Mohny, S. E.; Toney, M. F.; Sood, A. K.; Salleo, A.; Pop, E. Uncovering the Effects of Metal Contacts on Monolayer MoS₂. *ACS Nano* **2020**, *14* (11), 14798–14808.
- (2) Li, Y.; Yu, C.; Gan, Y.; Jiang, P.; Yu, J.; Ou, Y.; Zou, D.-F.; Huang, C.; Wang, J.; Jia, T.; Luo, Q.; Yu, X.-F.; Zhao, H.; Gao, C.-F.; Li, J. Mapping the Elastic Properties of Two-Dimensional MoS₂ via Bimodal Atomic Force Microscopy and Finite Element Simulation. *NPJ Comput Mater* **2018**, *4* (1), 49.
- (3) Amani, M.; Chin, M. L.; Mazzoni, A. L.; Burke, R. A.; Najmaei, S.; Ajayan, P. M.; Lou, J.; Dubey, M. Growth-Substrate Induced Performance Degradation in Chemically Synthesized Monolayer MoS₂ Field Effect Transistors. *Appl Phys Lett* **2014**, *104*, 203506.
- (4) Kataria, S.; Wagner, S.; Cusati, T.; Fortunelli, A.; Iannaccone, G.; Pandey, H.; Fiori, G.; Lemme, M. C. Growth-Induced Strain in Chemical Vapor Deposited Monolayer MoS₂: Experimental and Theoretical Investigation. *Adv Mater Interfaces* **2017**, *4*, 1700031.
- (5) Luo, S.; Cullen, C. P.; Guo, G.; Zhong, J.; Duesberg, G. S. Investigation of Growth-Induced Strain in Monolayer MoS₂ Grown by Chemical Vapor Deposition. *Appl Surf Sci* **2020**, *508*, 145126.
- (6) English, C. D.; Shine, G.; Dorgan, V. E.; Saraswat, K. C.; Pop, E. Improved Contacts to MoS₂ Transistors by Ultra-High Vacuum Metal Deposition. *Nano Lett* **2016**, *16*, 3824–3830.
- (7) Schranghamer, T. F.; Sakib, N. U.; Sadaf, M. U. K.; Subbulakshmi Radhakrishnan, S.; Pendurthi, R.; Agyapong, A. D.; Stepanoff, S. P.; Torsi, R.; Chen, C.; Redwing, J. M.; Robinson, J. A.; Wolfe, D. E.; Mohny, S. E.; Das, S. Ultrascaled Contacts to Monolayer MoS₂ Field Effect Transistors. *Nano Lett* **2023**, *23*, 3426–3434.
- (8) Datye, I. M.; Daus, A.; Grady, R. W.; Brenner, K.; Vaziri, S.; Pop, E. Strain-Enhanced Mobility of Monolayer MoS₂. *Nano Lett* **2022**, *22*, 8052–8059.
- (9) Hosseini, M.; Elahi, M.; Pourfath, M.; Esseni, D. Strain Induced Mobility Modulation in Single-Layer MoS₂. *J Phys D Appl Phys* **2015**, *48*, 375104.
- (10) John, A. P.; Thenapparambil, A.; Thalakulam, M. Strain-Engineering the Schottky Barrier and Electrical Transport on MoS₂. *Nanotechnology* **2020**, *31*, 275703.
- (11) Chen, Y.; Ke, F.; Ci, P.; Ko, C.; Park, T.; Saremi, S.; Liu, H.; Lee, Y.; Suh, J.; Martin, L. W.; Ager, J. W.; Chen, B.; Wu, J. Pressurizing Field-Effect Transistors of Few-Layer MoS₂ in a Diamond Anvil Cell. *Nano Lett* **2017**, *17* (1), 194–199.
- (12) Manzanares-Negro, Y.; Quan, J.; Rassekh, M.; Moaied, M.; Li, X.; Ares, P.; Palacios, J. J.; Gomez-Herrero, J.; Gomez-Navarro, C. Low Resistance Electrical Contacts to Few-Layered MoS₂ by Local Pressurization. *2D Mater* **2023**, *10* (2), 021003.
- (13) Sohler, T.; Ponomarev, E.; Gibertini, M.; Berger, H.; Marzari, N.; Ubrig, N.; Morpurgo, A. F. Enhanced Electron-Phonon Interaction in Multivalley Materials. *Phys Rev X* **2019**, *9* (3), 031019.

- (14) Shen, P.-C.; Su, C.; Lin, Y.; Chou, A. S.; Cheng, C. C.; Park, J. H.; Chiu, M. H.; Lu, A. Y.; Tang, H. L.; Tavakoli, M. M.; Pitner, G.; Ji, X.; Cai, Z.; Mao, N.; Wang, J.; Tung, V.; Li, J.; Bokor, J.; Zettl, A.; Wu, C. I.; Palacios, T.; Li, L. J.; Kong, J. Ultralow Contact Resistance between Semimetal and Monolayer Semiconductors. *Nature* **2021**, *593*, 211–217.
- (15) Das, S.; Chen, H.-Y.; Penumatcha, A. V.; Appenzeller, J. High Performance Multilayer MoS₂ Transistors with Scandium Contacts. *Nano Lett* **2013**, *13*, 100–105.
- (16) Schroder, D. K. *Semiconductor Material and Device Characterization*, 3rd ed.; John Wiley & Sons, Inc., 2006.
- (17) Smithe, K. K. H.; Suryavanshi, S. V.; Muñoz Rojo, M.; Tedjarati, A. D.; Pop, E. Low Variability in Synthetic Monolayer MoS₂ Devices. *ACS Nano* **2017**, *11* (8), 8456–8463.
- (18) Dorow, C.; O'Brien, K.; Naylor, C. H.; Lee, S.; Penumatcha, A.; Hsiao, A.; Tronic, T.; Christenson, M.; Maxey, K.; Zhu, H.; Oni, A.; Alaan, U.; Gosavi, T.; Gupta, A. Sen; Bristol, R.; Clendenning, S.; Metz, M.; Avci, U. Advancing Monolayer 2-D NMOS and PMOS Transistor Integration from Growth to Van Der Waals Interface Engineering for Ultimate CMOS Scaling. *IEEE Trans Electron Devices* **2021**, *68*, 6592–6598.